

Deep Learning with a Single Neuron: Folding a Deep Neural Network in Time using Feedback-Modulated Delay Loops

Florian Stelzer^{1,2}, André Röhm³, Raul Vicente⁴, Ingo Fischer³, and Serhiy Yanchuk^{1,*}

¹Institute of Mathematics, Technische Universität Berlin, 10623, Germany

²Department of Mathematics, Humboldt-Universität zu Berlin, 12489, Germany

³Instituto de Física Interdisciplinar y Sistemas Complejos, IFISC (UIB-CSIC), Campus Universitat de les Illes Balears, E-07122 Palma de Mallorca, Spain

⁴Institute of Computer Science, University of Tartu, Tartu, Estonia

*corresponding author

Deep neural networks are among the most widely applied machine learning tools showing outstanding performance in a broad range of tasks. We present a method for folding a deep neural network of arbitrary size into a single neuron with multiple time-delayed feedback loops. This single-neuron deep neural network comprises only a single nonlinearity and appropriately adjusted modulations of the feedback signals. The network states emerge in time as a temporal unfolding of the neuron's dynamics. By adjusting the feedback-modulation within the loops, we adapt the network's connection weights. These connection weights are determined via a modified back-propagation algorithm that we designed for such types of networks. Our approach fully recovers standard Deep Neural Networks (DNN), encompasses sparse DNNs, and extends the DNN concept toward dynamical systems implementations. The new method, which we call *Folded-in-time DNN (Fit-DNN)*, exhibits promising performance in a set of benchmark tasks.

1 Introduction

Fueled by Deep Neural Networks (DNN), machine learning systems are achieving outstanding results in large-scale problems. The data-driven representations learned by DNNs empower state-of-the-art solutions to a range of tasks in computer vision, reinforcement learning, robotics, healthcare, and natural language processing [1, 2, 3, 4, 5, 6, 7, 8, 9]. Their success has also motivated the implementation of DNNs using alternative hardware platforms, such as photonic or electronic concepts, see, e.g., [10, 11, 12] and references therein. However, so far, these alternative hardware implementations require major technological efforts to realize partial functionalities, and, depending on the hardware platform, the corresponding size of the DNN remains rather limited [12].

Here, we introduce a folding-in-time approach to emulate a full DNN using only a single artificial neuron with feedback-modulated delay loops. Temporal modulation of the signals within the individual delay loops allows realizing adjustable connection weights among the hidden layers. This approach can reduce the required hardware drastically and offers a new perspective on how to construct trainable complex systems: The large network of many interacting elements is replaced by a single element, representing different elements in time by interacting with its own delayed states. We are able to show that our folding-in-time approach is fully equivalent to a feed-forward deep neural network under certain constraints—and that it, in addition, encompasses dynamical systems specific architectures. We name our approach *Folded-in-time Deep Neural Network* or short **Fit-DNN**.

Our approach follows an interdisciplinary mindset that draws its inspiration from the intersection of AI systems, brain-inspired hardware, dynamical systems, and analogue computing. Choosing such a different perspective on DNNs leads to a better understanding of their properties, requirements, and capabilities. In particular, we discuss the nature of our Fit-DNN from a dynamical systems' perspective. We derive an adapted back-propagation approach applicable to gradient descent training of Fit-DNNs based on continuous dynamical systems and demonstrate that it provides good performance results in a number of tasks. Our approach will open up new strategies to implement DNNs in alternative hardware.

For the related machine learning method called 'reservoir computing' based on fixed recurrent neural networks, folding-in-time concepts have already been successfully developed [13]. Delay-based reservoir computing typically uses a single delay loop configuration and time-multiplexing of the input data to emulate a ring topology. The introduction of this concept led to a better understanding of reservoir computing, its minimal requirements, and suitable parameter conditions. Moreover, it facilitated their implementation on various hardware platforms [13, 14, 15, 16, 17, 18, 19]. In fact, the delay-based reservoir computing concept inspired successful implementations in terms of hardware efficiency [13], processing speed [16, 20, 21], task performance [22, 23], and last, but not least, energy consumption [16, 22].

For DNN, a folding-in-time approach has been lacking so far. We present the Fit-DNN concept and show its versatility and applicability to solve real-world tasks.

2 Results

2.1 A network folded into a single neuron

The traditional Deep Neural Networks consist of multiple layers of neurons coupled in a feed-forward architecture. Implementing their functionality with only a single neuron requires preserving the logical order of the layers while finding a way to sequentialize the operation within the layer. This can only be achieved by temporally spacing out processes that previously acted simultaneously. A single neuron receiving the correct inputs at the correct times sequentially emulates each neuron in every layer. The connections that previously linked neighboring layers now instead have to connect the single neuron at different *times*, and thus interlayer links turn into *delay*-connections. The weight of these connections has to be adjustable, and therefore a temporal modulation of these connections is required.

The architecture derived this way is depicted in Fig. 1 and

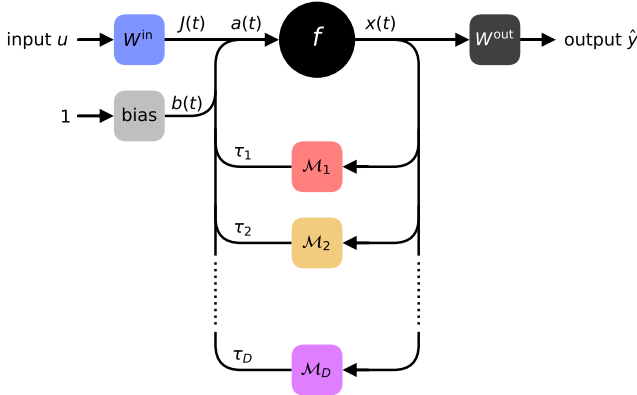


Figure 1: Scheme of the Fit-DNN setup. A nonlinear element (neuron) with a nonlinear function f is depicted by a black circle. The state of the neuron at time t is $x(t)$. The signal $a(t)$ is the sum of the data $J(t)$, bias $b(t)$, and feedback signals. Each feedback loop implements a delay τ_d and a temporal modulation $\mathcal{M}_d(t)$.

called Folded-in-time DNN. The core of the Fit-DNN consists of a single neuron with multiple delayed and modulated feedbacks. The type or exact nature of the single neuron is not essential; we only demand that its system state evolves in continuous time according to a differential equation of the general form:

$$\dot{x}(t) = -\alpha x(t) + f(a(t)), \quad \text{where} \quad (1)$$

$$a(t) = J(t) + b(t) + \sum_{d=1}^D \mathcal{M}_d(t)x(t - \tau_d). \quad (2)$$

Here $x(t)$ denotes the state of the neuron; f is a nonlinear function with the argument $a(t)$ combining the data signal $J(t)$, time-varying bias $b(t)$, and the time-delayed feedback signals $x(t - \tau_d)$ modulated by the functions $\mathcal{M}_d(t)$, see Fig. 1. We explicitly consider multiple loops of different delay lengths τ_d . Due to the feedback loops, the system becomes a so-called delay dynamical system, which leads to profound implications for the complexity of its dynamics [24, 25, 26, 27, 28, 29, 30, 31, 32].

Intuitively, the feedback loops in Fig. 1 lead to a reintroduction of information that has already passed through the nonlinearity f . This allows chaining the nonlinearity f many times. While a classical DNN composes its trainable representations by using neurons layer-by-layer, the Fit-DNN achieves the same by reintroducing a feedback signal to the same neuron repeatedly. In each pass, the time-varying bias $b(t)$ and the modulations $\mathcal{M}_d(t)$ on the delay-lines ensure that the time evolution of the system processes information in the desired way. To obtain the data signal $J(t)$ and output \hat{y} we need an appropriate pre- or postprocessing, respectively.

2.2 Equivalence to multi-layer neural networks

To further illustrate how the Fit-DNN is functionally equivalent to a multi-layer neural network, we present Fig. 2 showing the main conceptual steps for transforming the dynamics of a single neuron with multiple delay loops into a DNN. A sketch of the time-evolution of $x(t)$ is presented in Fig. 2a. This evolution is divided into time-intervals of length T , each emulating a hidden layer. In each of the intervals, we choose N points. We use a grid of equidistant timings with small temporal separation θ . For hidden layers with N nodes, it follows that $\theta = T/N$. At each of these temporal grid points $t_n = n\theta$, we treat the system state $x(t_n)$ as an independent variable. Each temporal grid point t_n will represent a node, and $x(t_n)$ its state. We furthermore assume that the data signal $J(t)$, bias $b(t)$, and

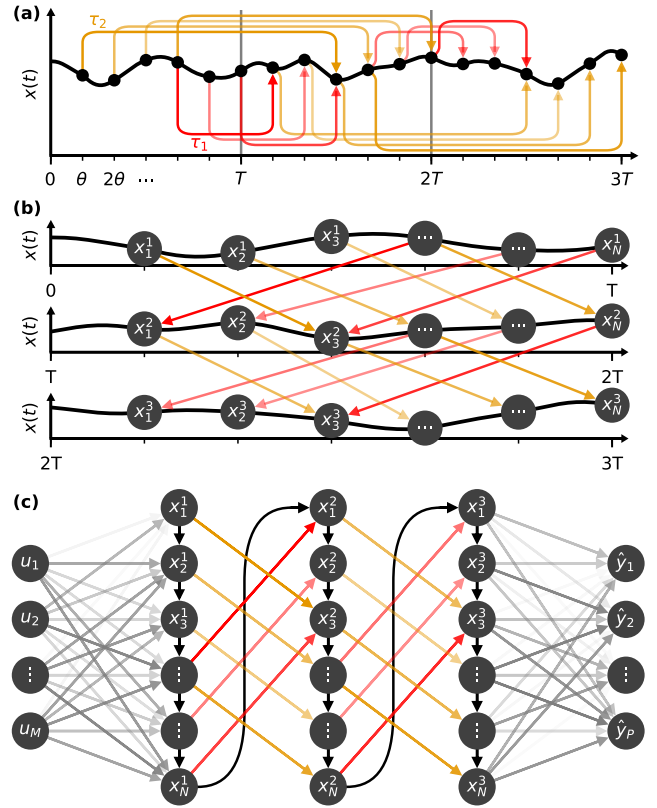


Figure 2: Equivalence of the Fit-DNN using a single neuron with modulated delayed feedbacks to a classical DNN. Panel (a): The neuron state is considered at discrete time points $x_n^\ell := x((\ell - 1)T + n\theta)$. The intervals $[(\ell - 1)T, \ell T]$ correspond to layers. Due to delayed feedbacks, non-local connections emerge (color lines). Panel (b) shows a stacked version of the plot in panel (a) with the same active connections. Panel (c) shows the resulting network: it is a rotated version of (b), with additional input and output layers. Black lines indicate connections implied by the temporal ordering of the emulation.

modulation signals $\mathcal{M}_d(t)$ are step functions with step-lengths θ ; we refer to the Methods Sec. 4 for their precise definitions.

By considering the dynamical evolution of the time-continuous system $x(t)$ only at these discrete temporal grid points t_n (black dots in Fig. 2a), one can prove that the Fit-DNN emulates a classical DNN. To show it formally, we define network nodes x_n^ℓ of the equivalent DNN as

$$x_n^\ell := x((\ell - 1)T + n\theta), \quad (3)$$

with $n = 1, \dots, N$ determining the node's position within the layer, and $\ell = 1, \dots, L$ determining the layer. Analogously, we define the activations a_n^ℓ of the corresponding nodes. Furthermore, we add an additional node $x_{N+1}^\ell := 1$ to take into account the bias. Thus, the points from the original time-intervals T are now described by the vector $x^\ell = (x_1^\ell, \dots, x_N^\ell)$. Figure 2b shows the original time-trace cut into intervals of length T and nodes labeled according to their network position. The representation in Fig. 2c is a rotation of Fig. 2b with the addition of an input and an output layer.

The connections are determined by the dynamical dependencies between the nodes x_n^ℓ . These dependencies can be explicitly calculated either for small or large distance θ . In the case of a large node separation θ , the relations between the network

nodes x_n^ℓ is of the familiar DNN shape:

$$x_n^\ell = \alpha^{-1} f(a_n^\ell), \quad (4)$$

$$a_n^\ell := W^\ell x_{n-1}^{\ell-1}. \quad (5)$$

System (4) is derived in detail in the Supplementary Information. The matrix W^ℓ describes the connections from layer $\ell - 1$ to ℓ and corresponds to the modulated delay-lines in the original single-neuron system. Each of the time-delayed feedback loops leads to a dependence of the state $x(t)$ on $x(t - \tau_d)$, see colored arrows in Fig. 2a. By way of construction, the length of each delay-loop is fixed. Since the order of the nodes (3) is tied to the temporal position, a fixed delay-line cannot connect arbitrary nodes. Rather, each delay-line is equivalent to one diagonal of the coupling matrix W^ℓ . Depending on the number of delay loops D , the network possesses a different connectivity level between the layers. A fully connected Fit-DNN requires $2N - 1$ modulated delay loops, i.e., our connectivity requirement scales *linearly* in the system size N and is entirely independent of L , promising a favorable scaling for hardware implementations.

The time-dependent modulation signals $\mathcal{M}_d(t)$ allow us to set the feedback strengths to zero at certain times. For this work, we limit ourselves to delayed feedback connections, which only link nodes from the neighboring layers, but in principle this limitation could be lifted if more exotic networks were desired. For a visual representation of the connections implied by two sample delay loops, see Fig. 2b and c. The mismatch between the delay τ_d and T determines, which nodes are connected by that particular delay-loop: For $\tau_d < T$ ($\tau_d > T$), the delayed feedback connects a node x_n^ℓ with another node $x_{i+1}^{\ell+1}$ in a subsequent layer with $n > i$ ($n < i$), shown with red (yellow) arrows in Fig. 2.

To complete the DNN picture, the activations for the first layer will be rewritten as $a^1 := g(a^{\text{in}}) := g(W^{\text{in}}u)$, where W^{in} is used in the preprocessing of $J(t)$. A final output matrix W^{out} is used to derive the activations of the output layer $a^{\text{out}} := W^{\text{out}}x^L$. We refer to the Methods Sec. 4.2 for a precise mathematical description.

2.3 Dynamical systems perspective: small node separation

For small node separation θ , the Fit-DNN approach goes beyond the standard DNN. Inspired by the method used in [13, 33, 34], we apply the variation of constants formula to solve the linear part of (1) and the Euler discretization for the non-linear part and obtain the following relations between the nodes up to the first-order terms in θ :

$$x_n^\ell = e^{-\alpha\theta} x_{n-1}^\ell + \alpha^{-1}(1 - e^{-\alpha\theta})f(a_n^\ell), \quad n = 2, \dots, N, \quad (6)$$

for the layers $\ell = 1, \dots, L$, and nodes $n = 2, \dots, N$. Note, how the first term $e^{-\alpha\theta} x_{n-1}^\ell$ couples each node to the preceding one within the same layer. Furthermore, the first node of each layer ℓ is connected to the last node of the preceding layer:

$$x_1^\ell = e^{-\alpha\theta} x_N^{\ell-1} + \alpha^{-1}(1 - e^{-\alpha\theta})f(a_1^\ell), \quad (7)$$

where $x_N^0 := x_0 = x(0)$ is the initial state of system (1). Such a dependence reflects the fact that the network was created from a single neuron with time-continuous dynamics. With insufficient node separation θ , each node state residually depends on the preceding one and is not fully independent. These additional ‘inertial’ connections are represented by the black arrows in the network representation in Fig. 2c and are present in the case of small θ .

This second case of small θ may seem like a spurious, superfluous regime that unnecessarily complicates the picture. However, in practice, a small θ directly implies a fast operation—

the time the single neuron needs to emulate a layer is directly given by $N\theta$. We, therefore, expect this regime to be of interest for future hardware implementations. Additionally, while we recover a fully connected DNN using $D = 2N - 1$ delay loops, our simulations show that this is not a strict requirement. Adequate performance can already be obtained with a much smaller number of delay loops. In that case, the Fit-DNN is implementing a particular type of sparse DNNs.

2.4 Back-propagation for Fit-DNN

The Fit-DNN (4) for large θ is the classical multilayer perceptron; hence, the weight gradients can be computed using the classical back-propagation algorithm [35, 36, 3]. However, if less than the full number of delay-loops is used, the resulting DNN will be sparse. Training sparse DNN is a current topic of research [37, 38], but as a first step, the traditional back-propagation algorithm can still be applied.

For a small temporal node separation θ , the Fit-DNN approach differs from the classical multilayer perceptron because it contains additional linear intra-layer connections and additional linear connections from the last node of one hidden layer to the first node of the next hidden layer, see Fig. 2c, black arrows. Nonetheless, the network can be trained by adjusting the input weights W^{in} , the output weights W^{out} , and the non-zero elements of the potentially sparse weight matrices W^ℓ using gradient descent. For this, we employ a modified back-propagation algorithm, described in Sec. 4.3, which takes these additional connections into consideration.

2.5 Benchmark tasks

Since under certain conditions, the Fit-DNN fully recovers a standard DNN (without convolutional layers), the resulting performance will be identical. This is obvious, when considering system (4), since the dynamics are perfectly described by a standard multilayer perceptron. However, the Fit-DNN approach also encompasses the aforementioned cases of short temporal node distance θ and the possibility of using less delay-loops, which translates to a sparse DNN. We report here that the system retains its computational power even in these regimes, i.e. a Fit-DNN can in principle be constructed with few and short delay-loops.

To demonstrate the computational capabilities of the Fit-DNN over these regimes, we considered four image classification tasks: MNIST [39], Fashion-MNIST [40], CIFAR-10 [41], and the cropped version of SVHN [42]. As a demonstration for a very sparse network, we applied the Fit-DNN to an image denoising task: We added Gaussian noise of intensity $\sigma_{\text{task}} = 1$ to the images of the Fashion-MNIST dataset, which we considered as vectors with values between 0 (white) and 1 (black). Then we clipped the resulting vector entries at the clipping thresholds 0 and 1 in order to obtain noisy grayscale images. The denoising task is to reconstruct the original images from their noisy versions. Figure 3 shows examples of the original Fashion-MNIST images, their noisy versions, and reconstructed images.

For the tests, we solved the delay system (1) numerically and trained the weights by gradient descent using the modified back-propagation algorithm described in Sec. 4.3. Unless noted otherwise, we operated in the small θ regime, and in general did not use a fully connected network. By nature of the architecture, the choice of delays τ_d is not trivial. We always chose the delays as a multiple of θ , i.e. $\tau_d = n_d\theta$, $d = 1, \dots, D$. The integer n_d can range from 1 to $2N - 1$ and indicates which diagonal of the weight matrix W^ℓ is accessed. After some initial tests, we settled on drawing the numbers n_d from a uniform distribution on the set $\{1, \dots, 2N - 1\}$ without replacement.

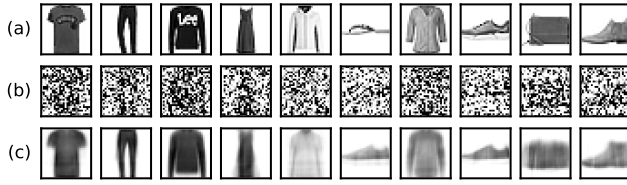


Figure 3: Example images for the denoising task. Row (a) contains original images from the Fashion-MNIST data set. Row (b) shows the same images with additional Gaussian noise. These noisy images serve as input data for the trained system. Row (c) shows the obtained reconstructions of the original images.

	(a)	(b)	(c)
input nodes M	784	3072	784
output nodes P	10	10	784
nodes per hidden layer N	100	100	100
number of hidden layers L	2	3	2
number of delays D	100	100	5
node separation θ	0.5	0.5	0.5
system time scale α	1	1	1
initial training rate η_0	0.01	0.0001	0.001
training rate scaling factor η_1	10000	1000	500
intensity of training noise σ	0.1	0.01	–

Table 1: Standard parameters for (a) the MNIST and Fashion-MNIST tasks, (b) the CIFAR-10 and cropped SVHN tasks, and (c) the image denoising task.

If not stated otherwise, we used the activation function $f(a) = \sin(a)$, but the Fit-DNN is in principle agnostic to the type of nonlinearity f that is used. The standard parameters for our numerical tests are listed in Table 1. For further details we refer to the Methods Sec. 4.4.

In Table 2, we show the Fit-DNN performance for different numbers of the nodes $N = 50, 100, 200$, and 400 per hidden layer on the aforementioned tasks. We immediately achieve high success rates on the relatively simple MNIST and Fashion-MNIST tasks. The more challenging CIFAR-10 and cropped SVHN tasks obtain lower yet still significant success rates. The confusion matrices (see Supplementary Information) also show that the system tends to confuse similar categories (e.g. ‘automobile’ and ‘truck’). While these results clearly do not rival record state-of-the-art performances, they were achieved on a novel and radically different architecture. In particular, the Fit-DNN here only used about half of the available diagonals of the weight matrix and operated in the small θ regime. For the tasks tested,

N	50	100	200	400
MNIST	97.31	98.49	98.91	98.97
Fashion-MNIST	86.61	87.82	88.59	89.18
CIFAR-10	48.29	51.42	53.94	54.99
cropped SVHN	73.45	78.93	80.85	81.38
denoising	0.0277	0.0254	0.0241	0.0236

Table 2: Fit-DNN performance for classification and denoising tasks; dependence on the number of nodes per hidden layer N . Shown are accuracies [in %] and mean squared error for the denoising task for different N . Increasing N improves the results for all tasks. For the classification tasks with $N = 50$, the number of delays is $D = 99$, for the other cases the standard value $D = 100$ is used. For the denoising task, $D = 5$ is used for all cases.

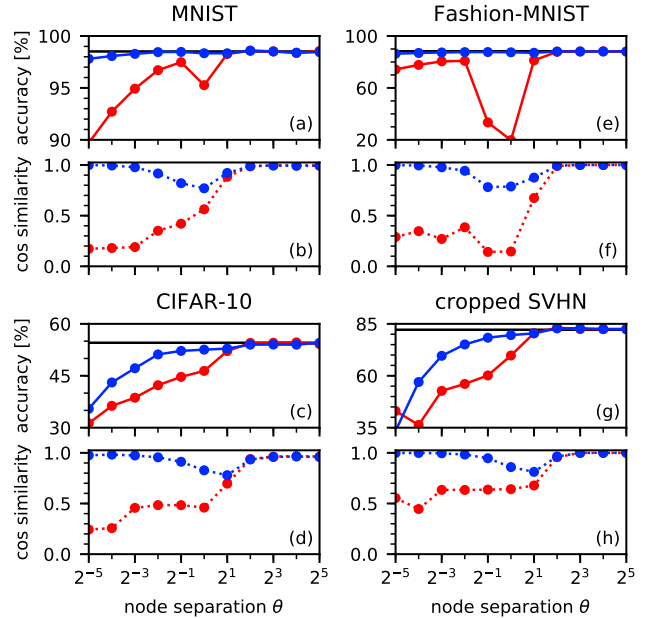


Figure 4: Fit-DNN performance for classification and denoising tasks; dependence on the node separation θ . Shown are accuracies of the classification tasks by employing the modified (blue points), and classical (red points) back-propagation algorithm; panels (a, c, e, and g). The accuracy obtained in the map limit case $\theta \rightarrow \infty$ is shown by the horizontal black line. Lower panels show the cosine similarities between the numerically computed approximation of the exact gradient and the gradient obtained from the modified (blue points) and classical (red) back-propagation method.

increasing N clearly leads to increased performance. This also serves as a sanity check and proves the scalability of the concept. In particular, note that if implemented in some form of dedicated hardware, increasing the number of nodes per layer N does not increase the number of components needed, solely the time required to run the system. Also note, that the denoising task was solved using only 5 delay-loops. For a network of 400 nodes, this results in an extremely sparse weight matrix W^ℓ . Nonetheless, the system performs well.

Figure 4 shows the performance of the Fit-DNN for the classification tasks and the correctness of the computed gradients for different node separations θ . Since this is one of the key parameters that controls the Fit-DNN, understanding its influences is of vital interest. We also use this opportunity to illustrate the difference between the modified and the classical back-propagation algorithm for the gradient descent. We applied gradient checking, i.e. the comparison to a numerically computed practically exact gradient, to determine the correctness of the gradient estimates obtained from both back-propagation methods. We also trained the map limit network (4) for comparison, corresponding to a (sparse) multilayer perceptron. In this way, we can also see how the additional intra-layer connections influence the performance for small θ .

The obtained results of Fig. 4 confirm the advantage of the modified back-propagation algorithm over the classical one for the Fit-DNN. Specifically, the modified back-propagation algorithm (blue points in Fig. 4) yields correct gradients for large node separations $\theta \geq 4$ and for small node separations $\theta \leq 0.125$. For intermediate node separations, we obtain a rather rough approximation of the gradient, but the cosine similarity between the actual gradient and its approximation is still

at least 0.8, i.e. the approximation is good enough to train effectively. In contrast, the classical back-propagation algorithm (red points in Fig. 4) only works for large node separations $\theta \geq 4$, where the system approaches the map limit. Consequently, we obtain competitive accuracies for the MNIST and the Fashion-MNIST tasks even for small θ if we use the modified back-propagation method. When we apply the Fit-DNN to the more challenging CIFAR-10 and cropped SVHN tasks, small node separations affect the accuracies negatively. However, we still observe a significant advantage of the modified over the classical algorithm.

Further numerical results regarding the number of hidden layers L , the number of delays D , and the role of the activation function f are presented in detail in the Supplementary Information. We find that the optimal choice of L depends on the node separation θ . Our findings suggest that for small θ , one should choose a smaller number of hidden layers than for the map limit case $\theta \rightarrow \infty$. The effect of the number of delays D depends on the task. We found that a small number of delays is sufficient for the denoising task: the mean squared error remains constant when varying D between 5 and 40. For the CIFAR-10 task, a larger number of delays is necessary to obtain optimal results. If we use the standard parameters from Table 1, we obtain the highest CIFAR-10 accuracy for $D = 125$ or larger. This could likely be explained by the different requirements of these tasks: While the main challenge for denoising is to filter out unwanted points, the CIFAR-10 task requires attention to detail. Thus, a higher number of delay-loops potentially helps the system to learn a more precise representation of the target classes. By comparing the Fit-DNN performance for different activation functions, we also confirmed that the system performs similarly well for the sine $f(a) = \sin(a)$, the hyperbolic tangent $f(a) = \tanh(a)$, and the ReLU function $f(a) = \max\{0, a\}$.

3 Discussion

We have designed a method for complete Folding-in-time of a multi-layer feed-forward DNN. This Fit-DNN approach requires only a single neuron with feedback-modulated delay-loops. Via a temporal sequentialization of the nonlinear operations, an arbitrarily deep or wide DNN can be realized. We also naturally arrive at slight modifications, such as sparse DNN or DNNs, which contain additional inertial connections. For this, we have developed a modified back-propagation method for gradient descent training of the coupling weights.

Even for the case of sparse connectivity, we can perform image classification using only a single dynamical neuron. This case, in particular, highlights one of the most exciting aspects of the Fit-DNN architecture: Many hardware implementations of DNNs or related systems have suffered from the large amount of elements that need to be implemented: the active neurons as well as the connections with adjustable weights. The Fit-DNN overcomes both of these limitations: no matter how many neurons are functionally desired, physically, we only require a single one. Even though we advocate for sparse connectivity in this paper, a fully connected DNN would require only linearly scaling the number of delay loops with the number of nodes per layer N . This is in strong contrast to directly implemented networks, where the number of connections grows quadratically. Where it is acceptable to use sparse networks, increasing the number of layers L or the number of nodes per layer N for the Fit-DNN only requires more time, but not more elements. At the same time, since only one nonlinear node and, in principle, one fast read-out element are absolutely required in our approach, ultrafast components might be used that would be unrealistic to use in full DNN implementations.

The Fit-DNN approach is agnostic concerning the type of

nonlinearity, enabling flexibility of implementations. A suitable candidate for such a hardware implementation could be a photonic neuromorphic implementation [13, 14, 15, 16, 43, 44, 20], where a fast artificial neuron can be realized with the Gigahertz timescale range. Photonic systems have already been used to construct delay-based reservoir computers, which is where the original idea of folding a neural network in time was first introduced [13]. The possibility of folding a recurrent network into a single element already had a profound effect on understanding these systems. In contrast to the folding-in-time of a recurrent network for reservoir computing, here we use the technique in a different way to realize a (multi-layer) feed-forward network architecture with adaptive connection weights. While more effort is required, the resulting Fit-DNN scheme can successfully represent a DNN and potentially go beyond those. Moreover, in retrospect, it is quite clear how instrumental the reduced hardware requirement of a delay-based approach was in stimulating the current ecosystem of reservoir computing implementations. We hope that for the much larger community around DNNs, a similar stimulating effect can be achieved with the Fit-DNN approach we presented here.

From a general perspective, our approach provides an alternative view on neural networks: the whole topological complexity of the feed-forward multilayer neural networks can be folded into the temporal domain by the delay-loop architecture. This uses the prominent advantage of time-delay systems that ‘space’ and ‘time’ can intermingle, and delay systems are known to possess rich spatio-temporal features [45, 32, 46, 47]. This work extends this spatio-temporal equivalence and its application significantly. Moreover, such an equivalence allows for the evaluation of neural networks with the tools of delay systems analysis [26, 30, 48, 49].

Our concept also differs clearly from the construction of neural networks from ordinary differential equations [50, 51, 52]. Our concept’s main advantage is that delay systems inherently possess an infinite-dimensional phase space. As a result, just one neuron is sufficient to fold the whole complexity of the network architecture.

We have presented a minimal and concise model, but already a multitude of potential extensions are apparent for future studies. For instance, one can implement different layer sizes, multiple nonlinear elements, and several other structures. Incorporating additional neurons (spatial nodes) might even enable finding the optimal trade-off between spatial and temporal nodes, depending on the chosen platform and task. Also, we envision building a hierarchical neural network consisting of interacting neurons, each of them folding a separate Fit-DNN in the temporal domain. Altogether, starting with the design used in this work, we might unlock a plethora of neural network architectures.

Finally, our approach encourages further cross-fertilization among different communities. While the spatio-temporal equivalence and the peculiar properties of delay-systems may be known in the dynamical systems community, so far, no application to DNNs had been considered. Conversely, the Machine Learning core idea is remarkably powerful, but usually not formulated to be compatible with continuous-time delay-dynamical systems. The Fit-DNN approach unifies these perspectives—and in doing so, provides a concept that is promising for those seeking a different angle to obtain a better understanding or to implement the functionality of DNNs in dedicated hardware.

4 Methods

4.1 The delay system and the signal $a(t)$

The delay system (1) is driven by a signal $a(t)$ which is defined by Eq. (2) as a sum of a data signal $J(t)$, modulated delayed feedbacks $\mathcal{M}_d(t)x(t - \tau_d)$, and a bias $b(t)$. In the following, we describe the components in detail.

(i) The input signal. Given an input vector $(u_1, \dots, u_M)^T \in \mathbb{R}^M$, a matrix $W^{\text{in}} \in \mathbb{R}^{N \times (M+1)}$ of input weights w_{nm}^{in} and an input scaling function g , we define

$$J(t) := g \left(w_{n,M+1}^{\text{in}} + \sum_{m=1}^M w_{nm}^{\text{in}} u_m \right), \quad (8)$$

for $(n-1)\theta < t \leq n\theta$ and $n = 1, \dots, N$. This rule defines the input signal $J(t)$ on the time interval $(0, T]$, whereas $J(t) = 0$ for the other values of t . Such a restriction ensures that the input layer connects only to the first hidden layer of the Fit-DNN. Moreover, $J(t)$ is a step function with the step lengths θ .

(ii) The feedback signals. System (1) contains D delayed feedback terms $\mathcal{M}_d(t)x(t - \tau_d)$ with the delay times $\tau_1 < \dots < \tau_D$, which are integer multiples of the stepsize $\tau_d = n_d\theta$, $n_d \in \{1, \dots, 2N-1\}$.

The modulation functions \mathcal{M}_d are defined interval-wise on the layer intervals $((\ell-1)T, \ell T]$. In particular, $\mathcal{M}_d(t) := 0$ for $t \leq T$. For $(\ell-1)T + (n-1)\theta < t \leq (\ell-1)T + n\theta$ with $\ell = 2, \dots, L$ and $n = 1, \dots, N$, we set

$$\mathcal{M}_d(t) := v_{d,n}^\ell. \quad (9)$$

Thus, the modulation functions $\mathcal{M}_d(t)$ are step functions with step length θ . The numbers $v_{d,n}^\ell$ play the role of the connection weights from layer $\ell-1$ to layer ℓ . More precisely, $v_{d,n}^\ell$ is the weight of the connection from the $(n+N-n_d)$ -th node of layer $\ell-1$ to the n -th node of layer ℓ . Section 4.2 below explains how the modulation functions translate to the hidden weight matrices W^ℓ . In order to ensure that the delay terms connect only consecutive layers, we set $v_{d,n}^\ell = 0$ whenever $n_d < n$ or $n_d > n + N - 1$ holds.

(iii) The bias signal. Finally, the bias signal $b(t)$ is defined as the step function

$$b(t) := b_n^\ell, \quad \text{for } (\ell-1)T + (n-1)\theta < t \leq (\ell-1)T + n\theta, \quad (10)$$

where $n = 1, \dots, N$ and $\ell = 2, \dots, L$. For $0 \leq t \leq T$, we set $b(t) := 0$ because the bias weights for the first hidden layer are already included in W^{in} , and thus in $J(t)$.

4.2 Network representation for small node separation θ

In this section, we provide details to the network representation of the Fit-DNN which was outlined in Sec. 2. The delay system (1) is considered on the time interval $[0, LT]$. As we have shown in Sec. 2, it can be considered as multi-layer neural network with L hidden layers, represented by the solution on sub-intervals of length T . Each of the hidden layers consists of N nodes. Moreover, the network possesses an input layer with M nodes and an output layer with P nodes. The input and hidden layers are derived from the system (1) by a discretization of the delay system with step length θ . The output layer is obtained by a suitable readout function on the last hidden layer.

We first construct matrices $W^\ell = (w_{nj}^\ell) \in \mathbb{R}^{N \times (N+1)}$, $\ell = 2, \dots, L$, containing the connection weights from layer $\ell-1$ to layer ℓ . These matrices are set up as follows: Let $n'_d := n_d - N$, then $w_{n,n-n'_d}^\ell := v_{d,n}^\ell$ define the elements of the matrices W^ℓ . All other matrix entries (except the last column) are defined to be zero. The last column is filled with the bias weights $b_1^\ell, \dots, b_N^\ell$. More specifically,

$$w_{nj}^\ell := \delta_{N+1,j} b_n^\ell + \sum_{d=1}^D \delta_{n-n'_d,j} v_{d,n}^\ell, \quad (11)$$

where $\delta_{n,j} = 1$ for $n = j$, and zero otherwise. The structure of the matrix W^ℓ is illustrated in the Supplementary Information.

Applying the variation of constants formula to system (1) yields for $0 \leq t_0 < t \leq TL$:

$$x(t) = e^{-\alpha(t-t_0)} x(t_0) + \int_{t_0}^t e^{\alpha(s-t)} f(a(s)) ds. \quad (12)$$

In particular, for $t_0 = (\ell-1)T + (n-1)\theta$ and $t = (\ell-1)T + n\theta$ we obtain

$$x_n^\ell = e^{-\alpha\theta} x_{n-1}^\ell + \int_{t_0}^{t_0+\theta} e^{\alpha(s-(t_0+\theta))} f(a(s)) ds, \quad (13)$$

where $a(s)$ is given by (2). Note that the functions $\mathcal{M}_d(t)$, $b(t)$, and $J(t)$ are step functions which are constant on the integration interval. Approximating $x(s - \tau_d)$ by the value on the right θ -grid point $x(t - \tau_d) \approx x((\ell-1)T + n\theta - n_d\theta)$ directly yields the network equation (6).

4.3 Application to machine learning and a modified back-propagation algorithm

We apply the system to two different types of machine learning tasks: image classification and image denoising. For the classification tasks, the size P of the output layer equals the number of classes. We choose f^{out} to be the softmax function, i.e.

$$\hat{y}_p = f_p^{\text{out}}(a^{\text{out}}) = \frac{\exp(a_p^{\text{out}})}{\sum_{q=1}^P \exp(a_q^{\text{out}})}, \quad p = 1, \dots, P. \quad (14)$$

If the task is to denoise a greyscale image, the number of output nodes P is the number of pixels of the image. In this case, clipping at the bounds 0 and 1 is a proper choice for f^{out} , i.e.

$$\hat{y}_p = f_p^{\text{out}}(a^{\text{out}}) = \begin{cases} 0, & \text{if } a_p^{\text{out}} < 0, \\ a_p^{\text{out}}, & \text{if } 0 \leq a_p^{\text{out}} \leq 1, \\ 1, & \text{if } a_p^{\text{out}} > 1. \end{cases} \quad (15)$$

‘Training the system’ means finding a set of training parameters, denoted by the vector \mathcal{W} , which minimizes a given loss function $\mathcal{E}(\mathcal{W})$. Our training parameter vector \mathcal{W} contains the input weights w_{nm}^{in} , the non-zero hidden weights w_{nj}^ℓ , and the output weights w_{pn}^{out} . The loss function must be compatible with the problem type and with the output activation. For the classification task, we use the cross-entropy loss function

$$\mathcal{E}_{\text{CE}}(\mathcal{W}) := - \sum_{k=1}^K \sum_{p=1}^P y_p(k) \ln(\hat{y}_p(k)) = - \sum_{k=1}^K \ln(\hat{y}_{p_t(k)}(k)), \quad (16)$$

where K is the number of examples used to calculate the loss and $p_t(k)$ is the target class of example k . For the denoising tasks, we use the rescaled mean squared error (MSE)

$$\mathcal{E}_{\text{MSE}}(\mathcal{W}) := \frac{1}{2K} \sum_{k=1}^K \sum_{p=1}^P (\hat{y}_p(k) - y_p(k))^2. \quad (17)$$

We train the system by stochastic gradient descent, i.e. for a sequence of training examples $(u(k), y(k))$ we modify the training parameter iteratively by the rule

$$\mathcal{W}_{k+1} = \mathcal{W}_k - \eta(k) \nabla \mathcal{E}(\mathcal{W}_k, u_k, y_k), \quad (18)$$

where $\eta(k) := \min(\eta_0, \eta_1/k)$ is a decreasing training rate.

If the node separation θ is sufficiently large, the local connections within the network become insignificant, and the gradient $\nabla \mathcal{E}(\mathcal{W})$ can be calculated using the classical back-propagation algorithm. Our numerical studies show that this works well if $\theta \geq 8$ for the considered examples. For smaller node separations, we need to employ a modified back-propagation algorithm. In the following, we briefly describe and compare both methods.

The classical back-propagation algorithm is derived by considering a multilayer neural network as a composition of functions

$$\hat{y} = f^{\text{out}}(a^{\text{out}}(a^L(\dots(a^1(a^{\text{in}}(u)))))) \quad (19)$$

and applying the chain rule. The first part of the algorithm is to iteratively compute partial derivatives of the loss function w.r.t. the node activations, the so called δ -terms

$$\delta_p^{\text{out}} := \partial_p \mathcal{E}(a^{\text{out}}) = \hat{y}_p - y_p, \quad (20)$$

$$\delta_n^L := \partial_n \mathcal{E}(a^L) = f'(a_n^L) \sum_{p=1}^P \delta_p^{\text{out}} w_{pn}^{\text{out}}, \quad (21)$$

$$\delta_n^\ell := \partial_n \mathcal{E}(a^\ell) = f'(a_n^\ell) \sum_{i=1}^N \delta_i^{\ell+1} w_{in}^\ell, \quad \ell = L-1, \dots, 1. \quad (22)$$

Then, the partial derivatives of the loss function w.r.t. the training parameters can be calculated:

$$\frac{\partial \mathcal{E}}{\partial w_{nm}^{\text{in}}} = \delta_n^1 u_m g'(a_n^{\text{in}}), \quad (23)$$

$$\frac{\partial \mathcal{E}}{\partial w_{nj}^\ell} = \delta_n^\ell x_j^{\ell-1}, \quad \ell = 2, \dots, L, \quad (24)$$

$$\frac{\partial \mathcal{E}}{\partial w_{pn}^{\text{out}}} = \delta_p^{\text{out}} x_n^L. \quad (25)$$

For details, see [53] or [3].

Taking the additional linear connections into account, we cannot consider a^ℓ as a function of $a^{\ell-1}$. Hence, we employ a modified approach to derive the back-propagation algorithm for this case. Our approach is to define extended activation vectors $\bar{a}^\ell \in \mathbb{R}^{N+1}$ with $\bar{a}_n^\ell := a_n^\ell$ for $n = 1, \dots, N$ and $\bar{a}_{N+1}^\ell := x_N^{\ell-1}$ for $\ell > 1$ and $\bar{a}_{N+1}^1 := x_0$. The extended activation vector \bar{a}^ℓ can be considered as a function of $\bar{a}^{\ell-1}$, thus we can apply the chain rule to the composition of functions

$$\hat{y} = f^{\text{out}}(a^{\text{out}}(\bar{a}^L(\dots(\bar{a}^1(a^{\text{in}}(u)))))). \quad (26)$$

We obtain the following algorithm:

Step 1: Compute

$$\Delta_p^{\text{out}} := \partial_p \mathcal{E}(a^{\text{out}}) = \delta_p^{\text{out}} = \hat{y}_p - y_p, \quad (27)$$

for $p = 1, \dots, P$.

Step 2: Let $\Phi := \alpha^{-1}(1 - e^{-\alpha\theta})$. Compute

$$\Delta_n^L := \partial_n \mathcal{E}(\bar{a}^L) = \Phi f'(a_n^L) \sum_{p=1}^P \Delta_p^{\text{out}} \sum_{j=n}^N w_{pj}^{\text{out}} e^{-\alpha\theta(j-n)}, \quad (28)$$

for $n = 1, \dots, N$, and

$$\Delta_{N+1}^L := \partial_{N+1} \mathcal{E}(\bar{a}^L) = \sum_{p=1}^P \Delta_p^{\text{out}} \sum_{j=1}^N w_{pj}^{\text{out}} e^{-\alpha\theta j}. \quad (29)$$

Step 3: For $\ell = L-1, \dots, 1$, compute

$$\Delta_n^\ell := \partial_n \mathcal{E}(\bar{a}^\ell) = \Phi f'(a_n^\ell) \left[\Delta_{N+1}^{\ell+1} e^{-\alpha\theta(N-n)} + \sum_{i=1}^N \Delta_i^{\ell+1} \sum_{j=n}^N w_{ij}^{\ell+1} e^{-\alpha\theta(j-n)} \right], \quad (30)$$

for $n = 1, \dots, N$, and

$$\Delta_{N+1}^\ell := \partial_{N+1} \mathcal{E}(\bar{a}^\ell) = \Delta_{N+1}^{\ell+1} e^{-\alpha\theta N} + \sum_{i=1}^N \Delta_i^{\ell+1} \sum_{j=1}^N w_{ij}^{\ell+1} e^{-\alpha\theta j}. \quad (31)$$

Step 4: Compute the partial derivatives w.r.t. the output weights

$$\frac{\partial \mathcal{E}}{\partial w_{pn}^{\text{out}}} = \Delta_p^{\text{out}} x_n^L. \quad (32)$$

for $n = 1, \dots, N+1$ and $p = 1, \dots, P$.

Step 5: Compute the partial derivatives w.r.t. the hidden weights

$$\frac{\partial \mathcal{E}}{\partial w_{nj}^\ell} = \Delta_n^\ell x_j^{\ell-1}, \quad (33)$$

for $j = 1, \dots, N+1$, $n = 1, \dots, N$ and $\ell = 2, \dots, L$.

Step 6: Compute the partial derivatives w.r.t. the input weights

$$\frac{\partial \mathcal{E}}{\partial w_{nm}^{\text{in}}} = \Delta_n^1 g'(a_n^{\text{in}}) u_m, \quad (34)$$

for $m = 1, \dots, M+1$ and $n = 1, \dots, N$.

For a detailed derivation of this algorithm we refer to the Supplementary Information.

4.4 Data augmentation, input processing and initialization

For all classification tasks, we performed an augmentation of the training input data by adding a small Gaussian noise to the images and by pixel jittering, i.e., randomly shifting the images by at most one pixel horizontally, vertically, or diagonally. For the CIFAR-10 task, we also applied a random rotation of maximal $\pm 15^\circ$ and a random horizontal flip with the probability 0.5 to the training input images. Further, we used dropout [54] with a dropout rate of 1% for the CIFAR-10 task. For the denoising task, we performed no data augmentation.

Moreover, for the four classification tasks, we used the input preprocessing function $g(a) = \tanh(a)$. For the denoising task, we applied no nonlinear input preprocessing, i.e. $g(a) = a$. The weights were always initialized by Xavier initialization [55]. In all cases, we used 100 training epochs.

Data availability

In this paper we built on four publicly available datasets: the MNIST dataset [39], the Fashion-MNIST dataset [40], the CIFAR-10 dataset [41], and the cropped version of the SVHN dataset [42]. All datasets are public and openly accessible online at <http://yann.lecun.com/exdb/mnist/>, <https://github.com/zalandoresearch/fashion-mnist>, <https://www.cs.toronto.edu/~kriz/cifar.html>, <http://ufldl.stanford.edu/housenumbers/>.

Code availability

The source code to reproduce the results of this study is freely available on GitHub: <https://github.com/flori-stelzer/deep-learning-delay-system>.

Acknowledgements

F.S. and S.Y. acknowledge funding by the "Deutsche Forschungsgemeinschaft" (DFG) in the framework of the project 411803875 and IRTG 1740. A.R. and I.F. acknowledge the Spanish State Research Agency, through the María de Maeztu Program for Units of Excellence in R & D (No. MDM-2017-0711). R.V. thanks the financial support from the Estonian Centre of Excellence in IT (EXCITE) funded by the European Regional Development Fund, through the research grant TK148.

Author Contributions

All authors contributed extensively to the work presented in this paper and to the writing of the manuscript.

Competing Interests statement

The authors declare no competing interests.

References

- [1] Lecun, Y., Bengio, Y. & Hinton, G. Deep learning. *Nature* **521**, 436–444 (2015).
- [2] Schmidhuber, J. Deep learning in neural networks: An overview. *Neural Networks* **61**, 85–117 (2015).
- [3] Goodfellow, I., Bengio, Y. & Courville, A. *Deep Learning* (MIT Press, Cambridge, Massachusetts, London, England, 2016).
- [4] Esteva, A. *et al.* Dermatologist-level classification of skin cancer with deep neural networks. *Nature* **542**, 115–118 (2017).
- [5] Jaderberg, M. *et al.* Human-level performance in 3d multiplayer games with population-based reinforcement learning. *Science* **364**, 859–865 (2019).
- [6] Neftci, E. O. & Averbeck, B. B. Reinforcement learning in artificial and biological systems. *Nature Machine Intelligence* **1**, 133–143 (2019).
- [7] Bonardi, A., James, S. & Davison, A. J. Learning one-shot imitation from humans without humans. *IEEE Robotics and Automation Letters* **5**, 3533–3539 (2020).
- [8] Wei, G. Protein structure prediction beyond alphafold. *Nature Machine Intelligence* **1**, 336–337 (2019).
- [9] Brown, T. B. *et al.* Language models are few-shot learners. Preprint at <https://arxiv.org/abs/2005.14165> (2020).
- [10] Misra, J. & Saha, I. Artificial neural networks in hardware: A survey of two decades of progress. *Neurocomputing* **74**, 239 – 255 (2010).
- [11] Schuman, C. D. *et al.* A survey of neuromorphic computing and neural networks in hardware. Preprint at <https://arxiv.org/abs/1705.06963> (2017).
- [12] De Marinis, L., Cococcioni, M., Castoldi, P. & Andriolli, N. Photonic neural networks: A survey. *IEEE Access* **7**, 175827–175841 (2019).
- [13] Appeltant, L. *et al.* Information processing using a single dynamical node as complex system. *Nat. Commun.* **2**, 468 (2011).
- [14] Larger, L. *et al.* Photonic information processing beyond Turing: an optoelectronic implementation of reservoir computing. *Optics Express* **20** (2012).
- [15] Duport, F., Schneider, B., Smerieri, A., Haelterman, M. & Massar, S. All-optical reservoir computing. *Optics Express* **20**, 22783–22795 (2012).
- [16] Brunner, D., Soriano, M. C., Mirasso, C. R. & Fischer, I. Parallel photonic information processing at gigabyte per second data rates using transient states. *Nature Communications* **4**, 1364 (2013).
- [17] Torrejon, J. *et al.* Neuromorphic computing with nanoscale spintronic oscillators. *Nature* **547**, 428–431 (2017).
- [18] Haynes, N. D., Soriano, M. C., Rosin, D. P., Fischer, I. & Gauthier, D. J. Reservoir computing with a single time-delay autonomous boolean node. *Phys. Rev. E* **91**, 020801 (2015).
- [19] Dion, G., Mejaouri, S. & Sylvestre, J. Reservoir computing with a single delay-coupled non-linear mechanical oscillator. *Journal of Applied Physics* **124**, 152132 (2018).
- [20] Larger, L. *et al.* High-speed photonic reservoir computing using a time-delay-based architecture: Million words per second classification. *Physical Review X* **7**, 1–14 (2017).
- [21] Bueno, J., Brunner, D., Soriano, M. C. & Fischer, I. Conditions for reservoir computing performance using semiconductor lasers with delayed optical feedback. *Optics Express* **25**, 2401–2412 (2017).
- [22] Vinckier, Q. *et al.* High-performance photonic reservoir computer based on a coherently driven passive cavity. *Optica* **2**, 438–446 (2015).
- [23] Argyris, A., Bueno, J. & Fischer, I. Pam-4 transmission at 1550 nm using photonic reservoir computing post-processing. *IEEE Access* **7**, 37017–37025 (2019).
- [24] Farmer, J. D. Chaotic attractors of an infinite-dimensional dynamical system. *Physica D* **4**, 366–393 (1982).
- [25] Le Berre, M. *et al.* Conjecture on the dimensions of chaotic attractors of delayed-feedback dynamical systems. *Physical Review A* **35**, 4020–4022 (1987).
- [26] Diekmann, O., Verduyn Lunel, S. M., van Gils, S. A. & Walther, H.-O. *Delay Equations* (Springer, New York, 1995).
- [27] Wu, J. *Introduction to Neural Dynamics and Signal Transmission Delay* (Walter de Gruyter, Berlin, Boston, 2001).
- [28] Erneux, T. *Applied Delay Differential Equations* (Springer, New York, 2009).
- [29] Atay, F. M. (ed.) *Complex Time-Delay Systems* (Springer, Berlin, 2010).
- [30] Michiels, W. & Niculescu, S.-I. *Stability, Control, and Computation for Time-Delay Systems* (Society for Industrial and Applied Mathematics, Philadelphia, 2014).

- [31] Erneux, T., Javaloyes, J., Wolfrum, M. & Yanchuk, S. Introduction to Focus Issue: Time-delay dynamics. *Chaos: An Interdisciplinary Journal of Nonlinear Science* **27**, 114201 (2017).
- [32] Yanchuk, S. & Giacomelli, G. Spatio-temporal phenomena in complex systems with time delays. *Journal of Physics A: Mathematical and Theoretical* **50**, 103001 (2017).
- [33] Schumacher, J., Toutounji, H. & Pipa, G. An analytical approach to single node delay-coupled reservoir computing. In *Artificial Neural Networks and Machine Learning – ICANN 2013*, 26–33 (Springer Berlin Heidelberg, Berlin, Heidelberg, 2013).
- [34] Stelzer, F., Röhm, A., Lüdge, K. & Yanchuk, S. Performance boost of time-delay reservoir computing by non-resonant clock cycle. *Neural Networks* **124**, 158–169 (2020).
- [35] Werbos, P. J. Applications of advances in nonlinear sensitivity analysis. In *System Modeling and Optimization: Proceedings of the 10th IFIP Conference*, 762–770 (Springer, Berlin, Heidelberg, 1982).
- [36] Rumelhart, D., Hinton, G. E. & Williams, R. J. Learning representations by back-propagating errors. *Nature* **323**, 533–536 (1986).
- [37] Mocanu, D., Mocanu, E., Stone, P. & et al. Scalable training of artificial neural networks with adaptive sparse connectivity inspired by network science. *Nat Commun* **9**, 2383 (2018).
- [38] Ardakani, A., Condo, C. & Gross, W. J. Sparsely-connected neural networks: Towards efficient VLSI implementation of deep neural networks. In *5th International Conference on Learning Representations, Conference Track Proceedings* (OpenReview.net, 2017).
- [39] Lecun, Y., Bottou, L., Bengio, Y. & Haffner, P. Gradient-based learning applied to document recognition. *Proceedings of the IEEE* **86**, 2278–2324 (1998).
- [40] Xiao, H., Rasul, K. & Vollgraf, R. Fashion-mnist: a novel image dataset for benchmarking machine learning algorithms. Preprint at <https://arxiv.org/abs/1708.07747> (2017).
- [41] Krizhevsky, A. Learning multiple layers of features from tiny images. *University of Toronto* (2012).
- [42] Netzer, Y. *et al.* Reading digits in natural images with unsupervised feature learning. *NIPS* (2011).
- [43] Van der Sande, G., Brunner, D. & Soriano, M. C. Advances in photonic reservoir computing. *Nanophotonics* **6**, 561–576 (2017).
- [44] Tanaka, G. *et al.* Recent advances in physical reservoir computing: A review. *Neural Networks* **115**, 100–123 (2019).
- [45] Giacomelli, G. & Politi, A. Relationship between Delayed and Spatially Extended Dynamical Systems. *Physical Review Letters* **76**, 2686–2689 (1996).
- [46] Hart, J. D., Schmadel, D. C., Murphy, T. E. & Roy, R. Experiments with arbitrary networks in time-multiplexed delay systems. *Chaos: An Interdisciplinary Journal of Nonlinear Science* **27**, 121103 (2017).
- [47] Hart, J. D., Larger, L., Murphy, T. E. & Roy, R. Delayed dynamical systems: networks, chimeras and reservoir computing. *Philosophical Transactions of the Royal Society A: Mathematical, Physical and Engineering Sciences* **377**, 20180123 (2019).
- [48] Sieber, J., Engelborghs, K., Luzyanina, T., Samaey, G. & Roose, D. Dde-biftool manual - bifurcation analysis of delay differential equations. Preprint at <https://arxiv.org/abs/1406.7144> (2016).
- [49] Breda, D., Diekmann, O., Gyllenberg, M., Scarabel, F. & Vermiglio, R. Pseudospectral discretization of nonlinear delay equations: New prospects for numerical bifurcation analysis. *SIAM Journal on Applied Dynamical Systems* **15**, 1–23 (2016).
- [50] Haber, E. & Ruthotto, L. Stable architectures for deep neural networks. *Inverse Problems* **34**, 014004 (2018).
- [51] Chen, R. T. Q., Rubanova, Y., Bettencourt, J. & Duvenaud, D. Neural ordinary differential equations. In *Proceedings of the 32nd International Conference on Neural Information Processing Systems*, 6572–6583 (Curran Associates Inc., Red Hook, NY, USA, 2018).
- [52] Lu, Y., Zhong, A., Li, Q. & Dong, B. Beyond finite layer neural networks: Bridging deep architectures and numerical differential equations. In *6th International Conference on Learning Representations, ICLR 2018 - Workshop Track Proceedings*, 3276–3285 (PMLR, Stockholm, Sweden, 2018).
- [53] Bishop, C. M. *Pattern Recognition and Machine Learning* (Springer, New York, 2006).
- [54] Srivastava, N., Hinton, G., Krizhevsky, A., Sutskever, I. & Salakhutdinov, R. Dropout: A simple way to prevent neural networks from overfitting. *Journal of Machine Learning Research* **15**, 1929–1958 (2014).
- [55] Glorot, X. & Bengio, Y. Understanding the difficulty of training deep feedforward neural networks. *Journal of Machine Learning Research - Proceedings Track* **9**, 249–256 (2010).

Deep Learning with a Single Neuron: Folding a Deep Neural Network in Time using Feedback-Modulated Delay Loops

Supplementary Information

Florian Stelzer^{1,2}, André Röhm³, Raul Vicente⁴, Ingo Fischer³, and Serhiy Yanchuk¹

¹Institute of Mathematics, Technische Universität Berlin, 10623, Germany

²Department of Mathematics, Humboldt-Universität zu Berlin, 12489, Germany

³Instituto de Física Interdisciplinar y Sistemas Complejos, IFISC (UIB-CSIC), Campus Universitat de les Illes Balears, E-07122 Palma de Mallorca, Spain

⁴Institute of Computer Science, University of Tartu, Tartu, Estonia

1 Fit-DNN performance and confusion matrices for different number of hidden layers, choice of delays, and the activation functions

Table 1 shows how the number of hidden layers L affects the performance of the Fit-DNN. We investigated two cases: the map limit $\theta \rightarrow \infty$ and the case $\theta = 0.5$. If the system operates in the map limit, we observe the optimal number of hidden layers 2 or 3, depending on the task. If $\theta = 0.5$, the performance of the Fit-DNN drops significantly for the CIFAR-10 [1], the cropped SVHN [2], and the denoising task. For this reason, deeper networks do not offer an advantage for solving these tasks if $\theta = 0.5$. The MNIST [3] and Fashion-MNIST [4] accuracies do not suffer much from choosing a small node separation θ . Here the systems performance remains almost unchanged in comparison to the map limit.

Figure 1 shows the effect of the choice of the number of delays D on the performance of the Fit-DNN. A larger number of delays D yields a slightly better accuracy for the CIFAR-10 task. We obtain an accuracy of less than 51% for $D = 25$, and an accuracy between 52% and 53% for $D = 125$ or larger. For the denoising task, we already obtain a good mean squared error (MSE) for small number of delays D . The MSE remains mostly between 0.0253 and 0.0258 independently of D . The fluctuations of the MSE are small.

We compare two methods for choosing the delays $\tau_d = n_d \theta$. The first method is to draw the numbers n_d without replacement from a uniform distribution on the set $\{1, \dots, 2N - 1\}$. The second method is to choose equidistant delays, with $n_{d+1} - n_d = \lfloor (2N - 1)/D \rfloor$. For the CIFAR-10 task, one may observe a slight advantage of the equidistant delays, whereas for the denoising task, randomly chosen delays yield slightly better results. In both cases, however, the influence of the chosen method on the quality of the results is small and seems to be insignificant.

Table 2 compares the performance of the Fit-DNN for different activation functions $f(a) = \sin(a)$, $f(a) = \tanh(a)$, and $f(a) = \max(0, a)$ (ReLU). The results show that the Fit-DNN works well with various activation functions.

Figure 2 shows the confusion matrices for the cropped SVHN and the CIFAR-10 tasks. These matrices show how often images of a corresponding dataset class are either recognized correctly or mismatched with another class. Confusion matrices are a suitable tool to identify which classes are confused more or less often. The confusion matrix for the cropped SVHN task shows, e.g., that the number 3 is relatively often falsely recognized as 5 or 9, but almost never as 4 or 6. The confusion matrix for the CIFAR-10 task indicates that images from animal classes (bird, cat, deer, dog, frog, horse) are often mismatched with another animal class, but rarely with a transportation class (airplane, automobile, ship, truck). This is an expected result for the CIFAR-10 task.

	L	1	2	3	4
$\theta = 0.5$	MNIST	98.43	98.54	98.3	98.24
	Fashion-MNIST	87.61	87.87	87.51	87.44
	CIFAR-10	52.35	52.13	52.05	51.32
	cropped SVHN	78.26	78.78	78.21	78.39
	denoising ($D = 5$)	0.0250	0.0254	0.0269	0.0362
	denoising ($D = 50$)	0.0251	0.0253	0.0269	0.0278
map limit	MNIST	98.41	98.62	98.47	98.58
	Fashion-MNIST	87.22	87.91	87.97	87.88
	CIFAR-10	53.69	54.57	54.28	54.15
	cropped SVHN	80.38	82.71	82.92	82.22
	denoising ($D = 5$)	0.0255	0.0244	0.0246	0.0250
	denoising ($D = 50$)	0.0257	0.0241	0.0243	0.0246

Table 1: Accuracies [%] for the classification tasks and mean squared error for the denoising task for different numbers of hidden layers L . For a node separation of $\theta = 0.5$, two hidden layers seem to be optimal for the classification tasks (except CIFAR-10), and one hidden layer is sufficient for the denoising task. When the systems operates in the map limit $\theta \rightarrow \infty$, additional hidden layers can improve the performance.

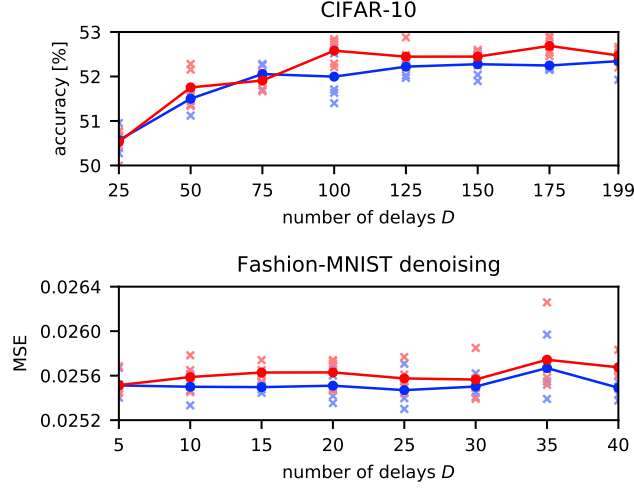


Figure 1: Accuracy and MSE for different numbers of delays D . For each D , the plots show 5 results (cross symbols) with delays drawn from uniform distribution (blue), and equidistant delays (red). The circle symbols connected by solid lines show the mean of the results.

f	sin	tanh	ReLU
MNIST	98.396	98.611	98.833
Fashion-MNIST	87.921	88.78	89.177
CIFAR-10	52.062	51.039	50.598
cropped SVHN	78.292	77.739	77.916
denoising	0.0254	0.0249	0.0255

Table 2: Accuracies [%] for the classification tasks and mean squared error for the denoising task for different activation functions f . Overall, the compared activation functions work similarly well.

Figure 3 shows results for a sine function fitting task. The objective of the task was to fit functions $y_i(u)$, $i = 1, \dots, 5$, $u \in [-1, 1]$, plotted in Fig. 4, which are defined as concatenations $y_i(u) = s_i \circ \dots \circ s_1(u)$ of sine functions $s_i(u) = \sin(\omega_i(u) + \varphi_i)$ with

$$\omega_1 = 0.65 \cdot 2\pi, \quad \omega_2 = 0.4 \cdot 2\pi, \quad \omega_3 = 0.3 \cdot 2\pi, \quad \omega_4 = 0.55 \cdot 2\pi, \quad \omega_5 = 0.45 \cdot 2\pi \quad (1)$$

$$\varphi_1 = 1.0, \quad \varphi_2 = -0.5, \quad \varphi_3 = -0.3, \quad \varphi_4 = 0.6, \quad \varphi_5 = 0.2. \quad (2)$$

The simulations were performed with $N = 20$ nodes per hidden layer, $D = 3$, and $\tau_1 = 15$, $\tau_2 = 20$, $\tau_3 = 25$. Since the task is to fit a concatenation of i sine functions and the Fit-DNN consists in this case of L concatenated sine functions, one would expect optimal results for $L \geq i$. In our tests, this was true up to $i = 3$. The function y_1 can be approximated by the Fit-DNN's output with a small MSE with any number of layers, see Fig. 3. The function y_2 can be fitted with a small error if and only if $L \geq 2$ (with a few exceptions). For the function y_3 we obtain relatively exact approximations with 2 or more hidden layers, but the smallest MSE is obtained with $L = 3$ in the most cases. The Fit-DNN fails to fit the functions y_4 and y_5 for all L .

2 The Fit-DNN delay system and map representation

2.1 Generating delay system

The Fit-DNN has M input nodes, P output nodes, and L hidden layers, each consisting of N nodes. The hidden layers are described by the delay system

$$\dot{x}(t) = -\alpha x(t) + f(a(t)), \quad (3)$$

$$a(t) = J(t) + b(t) + \sum_{d=1}^D \mathcal{M}_d(t)x(t - \tau_d), \quad (4)$$

where $\alpha > 0$ is a constant time-scale, f is a nonlinear activation function, and the argument $a(t)$ is a signal, which is composed of a data signal $J(t)$, a bias signal $b(t)$ and delayed feedback terms modulated by functions $\mathcal{M}_d(t)$. The components of $a(t)$ are described in the Methods Section. The delays are given by $\tau_d = n_d\theta$, where $\theta := T/N$ and $1 \leq n_1 < \dots < n_D \leq 2N - 1$ are natural numbers. The state of the ℓ -th hidden layer is given by the solution $x(t)$ of (3)–(4) on the interval $(\ell - 1)T < t \leq T$. We define the node states of the hidden layers as follows:

$$x_n^\ell := x((\ell - 1)T + n\theta) \quad (5)$$

for the node $n = 1, \dots, N$ of layer $\ell = 1, \dots, L$.

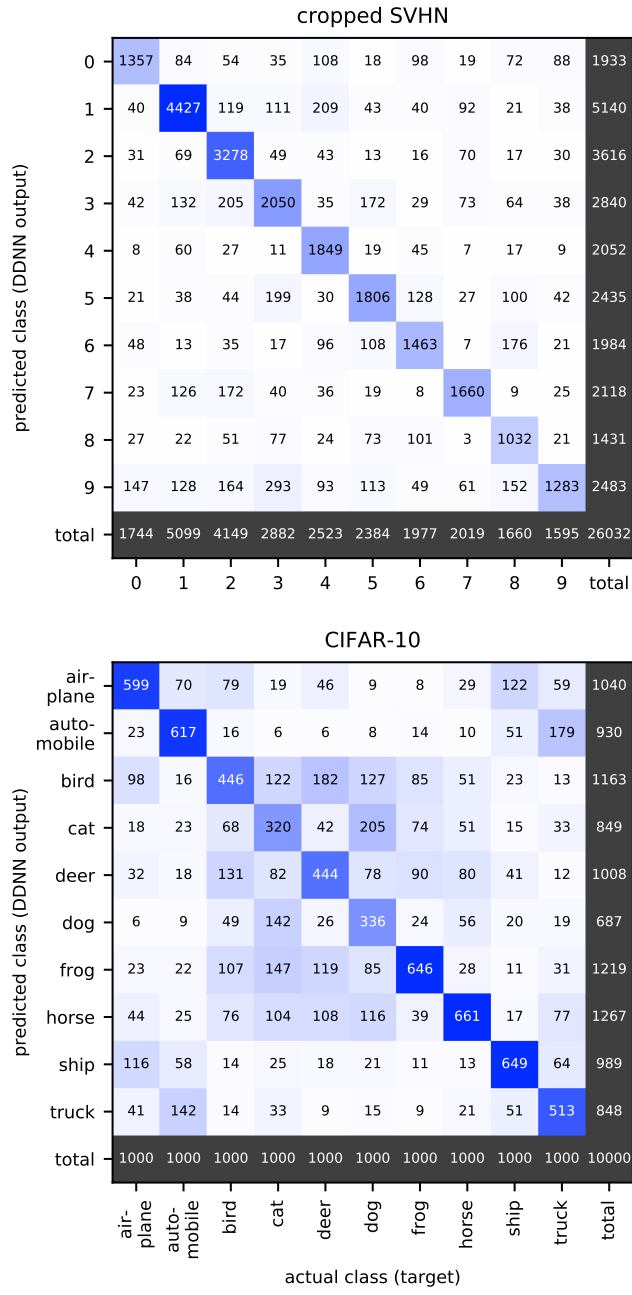


Figure 2: Numbers of images from the cropped SVHN and CIFAR-10 test sets by their actual class and the Fit-DNN's prediction. The CIFAR-10 confusion matrix implies that false predictions occur mostly within the superclasses *animals* and *transportation* but rarely between the superclasses.

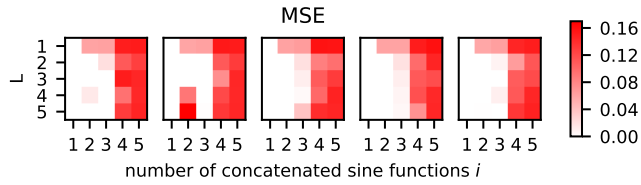


Figure 3: The plot shows the mean squared errors (MSE) for fitting the functions $y_i(u)$, $i = 1, \dots, 5$ with different numbers of layers L . We repeated the numerical experiment five times, each panel shows the results of one of these independent repetitions.

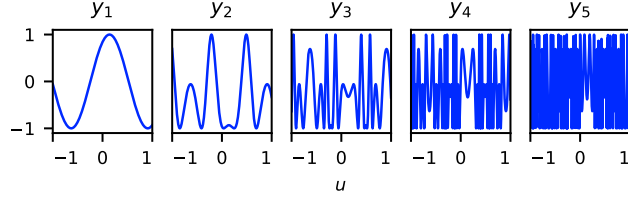


Figure 4: Functions $y_i(u)$, $i = 1, \dots, 5$.

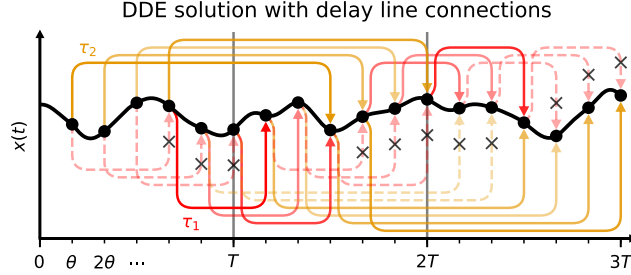


Figure 5: Solution of delay system (3)–(4) with delay-induced connections. Red arrows correspond to the delay $0 < \tau_1 < T$, and yellow to $T < \tau_2 < 2T$. Dashed lines with symbol \times indicate the removed connections due to the vanishing modulation amplitude (6).

The nodes of the hidden layers are connected by the delays τ_d , which is illustrated in Fig. 5. In order to ensure that only nodes of consecutive hidden layers are connected, we set

$$\mathcal{M}_d(t) = 0 \quad \text{if } t \in ((\ell - 1)T, \ell T] \text{ and } t - \tau_d = t - n_d\theta \notin ((\ell - 2)T, (\ell - 1)T]. \quad (6)$$

The delay connections, which are set to zero by condition (6), are indicated by dashed arrows marked with a black \times symbol in Fig. 5.

Additionally, we set $\mathcal{M}_d(t) = 0$ for $t \in [0, T]$. This implies, in combination with condition (6), that the system has no incoming delay connection from a time $t - \tau_d$ before zero. For this reason, we do not need to know a history function [5, 6, 7, 8] for the delay system (3)–(4) to compute the solution for positive time. Knowing the initial condition $x(0) = x_0$ at a single point is sufficient.

System (3)–(4) is defined on the interval $[0, LT]$. Applying the variation of constants formula yields for $0 \leq t_0 < t \leq LT$ the equation

$$x(t) = e^{-\alpha(t-t_0)}x(t_0) + \int_{t_0}^t e^{\alpha(s-t)}f(a(s))ds. \quad (7)$$

Using this equation on appropriate time intervals $[(n-1)\theta, n\theta]$, we obtain the following relations for the nodes in the first hidden layer

$$x_1^1 = e^{-\alpha\theta}x_0 + \int_0^\theta e^{\alpha(s-\theta)}f(a(s))ds, \quad (8)$$

$$x_n^1 = e^{-\alpha\theta}x_{n-1}^1 + \int_0^\theta e^{\alpha(s-\theta)}f(a((n-1)\theta + s))ds, \quad n = 2, \dots, N, \quad (9)$$

Here $x_0 = x(0)$ is the initial state of system (3)–(4). Similarly, for the hidden layers $\ell = 2, \dots, L$, we have

$$x_1^\ell = e^{-\alpha\theta}x_N^{\ell-1} + \int_0^\theta e^{\alpha(s-\theta)}f(a((\ell-1)T + s))ds, \quad (10)$$

$$x_n^\ell = e^{-\alpha\theta}x_{n-1}^\ell + \int_0^\theta e^{\alpha(s-\theta)}f(a((\ell-1)T + (n-1)\theta + s))ds, \quad n = 2, \dots, N. \quad (11)$$

For the first hidden layer, the signal $a(t)$ is piecewise constant. More specifically,

$$a(s) = J(s) = a_n^1 = g(a_n^{\text{in}}), \quad (n-1)\theta < s \leq \theta, \quad n = 1, \dots, N, \quad (12)$$

where

$$a^{\text{in}} = w_{n,M+1}^{\text{in}} + \sum_{m=1}^M w_{nm}^{\text{in}}u_m. \quad (13)$$

Taking into account (12), relations (8)–(9) lead to the following exact expressions for the nodes of the first hidden layer:

$$x_1^1 = e^{-\alpha\theta}x_0 + \alpha^{-1}(1 - e^{-\alpha\theta})f(a_1^1), \quad (14)$$

$$x_n^1 = e^{-\alpha\theta}x_{n-1}^1 + \alpha^{-1}(1 - e^{-\alpha\theta})f(a_n^1), \quad n = 2, \dots, N. \quad (15)$$

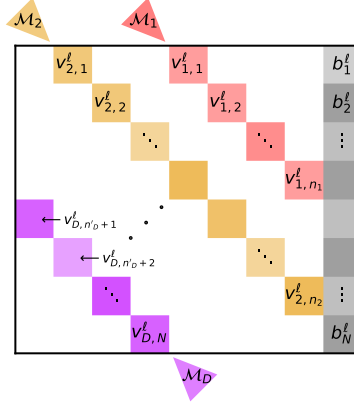


Figure 6: Illustration of the sparse weight matrix W^ℓ containing the connection weights between the hidden layers $\ell - 1$ and ℓ , see Eq. (20). The nonzero weights are arranged on diagonals, and equal to the values $v_{d,n}^\ell$ of functions \mathcal{M}_d . The position of the diagonals is determined by the corresponding delays τ_d . If $\tau_d = N\theta = T$, then the main diagonal contains the entries $v_{d,1}^\ell, \dots, v_{d,N}^\ell$. If $\tau_d = n_d\theta < T$, then the corresponding diagonal lies above the main diagonal and contains the values $v_{d,1}^\ell, \dots, v_{d,n_d}^\ell$. If $\tau_d = n_d\theta > T$, then the corresponding diagonal lies below the main diagonal and contains the values $v_{d,n'_d+1}^\ell, \dots, v_{d,N}^\ell$, where $n'_d = n_d - N$. The last column of the matrix contains the bias weights.

2.2 Map representation for small node separations

For the hidden layers $\ell = 2, \dots, L$, i.e. for $T < t \leq LT$, the signal $a(t)$ is defined as

$$a(t) = b(t) + \sum_{d=1}^D \mathcal{M}_d(t)x(t - \tau_d), \quad (16)$$

where $b(t)$ and $\mathcal{M}_d(t)$ are piecewise constant functions with discontinuities at the grid points $n\theta$. However, the dependence of $x(t - \tau_d)$ on time is not piecewise constant. Therefore, we cannot replace $a((\ell - 1)T + (n - 1)\theta + s)$, $0 < s < \theta$, in Eq. (10) and (11) by constants. However, if the node separation θ is small, we can approximate the value of

$$x((\ell - 1)T + (n - 1)\theta + s - \tau_d) = x((\ell - 1)T + (n - n_d - 1)\theta + s), \quad 0 < s < \theta, \quad (17)$$

at $s = \theta$, i.e., by the value $x((\ell - 1)T + n\theta - \tau_d)$, which can be rewritten as

$$x((\ell - 1)T + n\theta - \tau_d) = x((\ell - 1)T + (n - n_d)\theta) = x((\ell - 2)T + (n - n'_d)\theta), \quad (18)$$

where $n'_d = n_d - N$. Condition (6) ensures that the layer $\ell - 1$ is connected only to the previous layer $\ell - 2$. Formally, it means the nonzero values $v_{d,n}^\ell$ of \mathcal{M}_d allow only such connections that $1 \leq n - n'_d \leq N$, i.e. $x((\ell - 2)T + (n - n'_d)\theta) = x_{n-n'_d}^{\ell-2}$. As a result, we can approximate $a((\ell - 1)T + (n - 1)\theta + s)$ for $0 < s < \theta$ by

$$a_n^\ell = \sum_{j=1}^{N+1} w_{nj}^\ell x_j^{\ell-1}, \quad n = 1, \dots, N, \quad \ell = 2, \dots, L, \quad (19)$$

where

$$w_{nj}^\ell := \delta_{N+1,j} b_n^\ell + \sum_{d=1}^D \delta_{n-n'_d,j} v_{d,n}^\ell \quad (20)$$

defines a weight matrix $W^\ell = (w_{nj}^\ell) \in \mathbb{R}^{N \times (N+1)}$ for the connections from layer $\ell - 1$ to layer ℓ . This matrix is illustrated in Fig. 6.

In summary, we obtain the following map representation of the Fit-DNN, illustrated in Fig. 7, which approximates the nodes states up to first order terms in θ . The first hidden layer is given by

$$x_1^1 = e^{-\alpha\theta} x_0 + \alpha^{-1}(1 - e^{-\alpha\theta})f(a_1^1), \quad (21)$$

$$x_n^1 = e^{-\alpha\theta} x_{n-1}^1 + \alpha^{-1}(1 - e^{-\alpha\theta})f(a_n^1), \quad n = 2, \dots, N. \quad (22)$$

The hidden layers $\ell = 2, \dots, L$ are given by

$$x_1^\ell = e^{-\alpha\theta} x_N^{\ell-1} + \alpha^{-1}(1 - e^{-\alpha\theta})f(a_1^\ell), \quad (23)$$

$$x_n^\ell = e^{-\alpha\theta} x_{n-1}^\ell + \alpha^{-1}(1 - e^{-\alpha\theta})f(a_n^\ell), \quad n = 2, \dots, N, \quad (24)$$

and the output layer is defined by

$$\hat{y}_p := f_p^{\text{out}}(a^{\text{out}}), \quad p = 1, \dots, P, \quad (25)$$

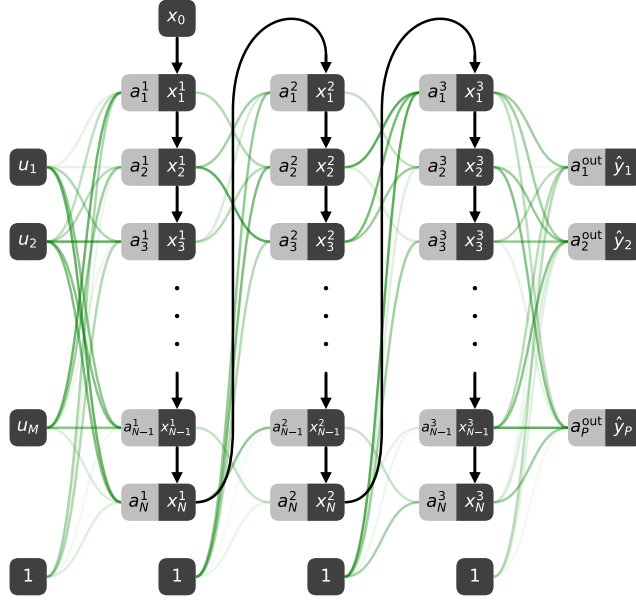


Figure 7: The multilayer neural network described by the equations (26)–(25). The connection weights which are subject to training are plotted in green. The connection weights between the input layer and the first hidden layer as well as the weights between the last hidden and the output layer are dense (all-to-all connection). The connections between the hidden layers are sparse. See Fig. 6 for an illustration of the connection matrices between the hidden layers. The difference to a classical multilayer perceptron are the linear connections between the nodes, which are plotted in black. These additional connections make it necessary to use a modified back-propagation method to compute the error gradients of the network. Note that also the hidden layers, specifically the nodes $x_{N-1}^{\ell-1}$ and x_1^{ℓ} , are directly linked by this type of additional linear connections. Thereby, the activation vectors $(a_1^{\ell}, \dots, a_N^{\ell})^T$ are skipped.

where f^{out} is an output activation function which suits to the given task. Moreover,

$$a_n^{\text{in}} := \sum_{m=1}^{M+1} w_{nm}^{\text{in}} u_m, \quad n = 1, \dots, N, \quad (26)$$

$$a_n^1 := g(a_n^{\text{in}}), \quad n = 1, \dots, N, \quad (27)$$

$$a_n^{\ell} := \sum_{j=1}^{N+1} w_{nj}^{\ell} x_j^{\ell-1}, \quad n = 1, \dots, N, \quad \ell = 2, \dots, L, \quad (28)$$

$$a_p^{\text{out}} := \sum_{n=1}^{N+1} w_{pn}^{\text{out}} x_n^L, \quad p = 1, \dots, P, \quad (29)$$

where $u_{M+1} := 1$ and $x_{N+1}^{\ell} := 1$, for $\ell = 1, \dots, L$. We call the a_n^{ℓ} and a_p^{out} the activation of the corresponding node. For $n = 1, \dots, N$, the variable w_{pn}^{out} denotes the output weight connecting the n -th node of layer L to the p -th output node, and $w_{p,(N+1)}^{\text{out}}$ denotes the bias for p -th output node (resp. the weight connecting the on-neuron x_{N+1}^L of layer L to the p -th output node).

The topology of the obtained map representation of the Fit-DNN does not depend on the discretization choice. Instead of following the above derivation, one could approximate the node states simply by applying an Euler scheme to the delay system (3)–(4). Then one obtains the map

$$x_n^{\ell} = x_{n-1}^{\ell} + \theta f(a_n^{\ell}), \quad (30)$$

which possesses the same connections as the map representation (21)–(29) of the Fit-DNN, but has slightly different connection weights. Nonetheless, for our purposes it is necessary to consider (21)–(29) instead of the simple Euler scheme (30). The weights $e^{-\alpha\theta}$ of the linear connections of neighboring nodes in Eq. (21)–(24) are only slightly smaller than the corresponding weights 1 in Eq. (30), but the indirect connection from x_n^{ℓ} to a distant node x_{ν}^{ℓ} with $\nu \gg n$ is $e^{-(\nu-n)\alpha\theta} \approx 0$. This fact helps us to calculate the error gradient of the Fit-DNN by the modified back-propagation algorithm derived in the section below. Using the simple Euler scheme, the connections weights between distant nodes remain to be 1.

2.3 Map limit

Here we show that the nodes of the Fit-DNN (8)–(11) can be approximated by the map limit

$$x_n^{\ell} = \alpha^{-1} f(a_n^{\ell}) \quad (31)$$

for large node separation θ , up to exponentially small terms $\mathcal{O}(e^{-\beta\theta})$ for all $0 < \beta < \alpha$. This limit corresponds to the approach for building networks of coupled maps from delay systems in [9, 10].

For the nodes of the first hidden layer, Eq. (14)–(15) provide exact solutions for any θ . Hence, replacing θ by $r \in [0, \theta]$, we obtain for the values of $x(t)$ in the interval $[(n-1)\theta, n\theta]$

$$x((n-1)\theta + r) = e^{-\alpha r} x_{n-1}^1 + \alpha^{-1}(1 - e^{-\alpha r})f(a_n^1), \quad (32)$$

which implies that the solution $x(t)$ decays exponentially to $f(a_n^1)$. In other words, it holds

$$x((n-1)\theta + r) = \alpha^{-1}f(a_n^1) + \mathcal{O}(e^{-\alpha r}). \quad (33)$$

In order to show similar exponential estimates for the layers $\ell = 2, \dots, L$, we use an inductive argument. For this, we assume that the following estimate holds for a layer $\ell - 1$:

$$x((\ell-2)T + (n-1)\theta + r) = \alpha^{-1}f(a_n^{\ell-1}) + \mathcal{O}(e^{-\beta r}) \quad (34)$$

for any constant $0 < \beta < \alpha$, $r \in [0, \theta]$, and all n within the layer. Note that this estimate is true for the first hidden layer, since (34) it is a weaker statement than (33). For the layer ℓ , we obtain from Eq. (7)

$$x((\ell-1)T + (n-1)\theta + r) = e^{-\alpha r} x_{n-1}^\ell + \int_0^r e^{\alpha(s-r)} f(a((\ell-1)T + (n-1)\theta + s)) ds, \quad (35)$$

where (34) implies

$$\begin{aligned} a((\ell-1)T + (n-1)\theta + s) &= b((\ell-1)T + (n-1)\theta + s) + \sum_{d=1}^D \mathcal{M}_d^\ell((\ell-1)T + (n-1)\theta + s)x((\ell-1)T + (n-1)\theta + s - \tau_d) \\ &= b_n^\ell + \sum_{d=1}^D v_{d,n}^\ell x((\ell-2)T + (n-1)\theta - n'_d\theta + s) \\ &= b_n^\ell + \sum_{d=1}^D v_{d,n}^\ell x((\ell-2)T + (n - n'_d)\theta) + \mathcal{O}(e^{-\beta s}) \\ &= a_n^\ell + \mathcal{O}(e^{-\beta s}). \end{aligned} \quad (36)$$

If f is Lipschitz continuous (which is the case for all our examples), it follows that

$$x((\ell-1)T + (n-1)\theta + r) = e^{-\alpha r} x_{n-1}^\ell + \alpha^{-1}(1 - e^{-\alpha r})f(a_n^\ell) + \int_0^r e^{\alpha(s-r)} \mathcal{O}(e^{-\beta s}) ds. \quad (37)$$

Since

$$\int_0^r e^{\alpha(s-r)} e^{-\beta s} ds = \frac{1}{\alpha - \beta} (e^{-\beta r} - e^{-\alpha r}) < \frac{e^{-\beta r}}{\alpha - \beta}, \quad (38)$$

we obtain

$$x((\ell-1)T + (n-1)\theta + r) = \alpha^{-1}f(a_n^\ell) + \mathcal{O}(e^{-\beta r}). \quad (39)$$

This holds in particular for $r = \theta$. Therefore we have shown that Eq. (31) holds up to terms of order $\mathcal{O}(e^{-\beta\theta})$ for any $0 < \beta < \alpha$.

3 Back-propagation for the Fit-DNN

The map representation (21)–(29) of the Fit-DNN, illustrated by Fig. 7, contains additional linear connections which do not occur in classical multilayer perceptrons. Thus, we cannot apply the classical back-propagation algorithm for the gradient computation necessary for the weight training. Instead, we derive a modified back-propagation algorithm which is specific for (21)–(29).

Firstly, we define extended activation vectors

$$\bar{a}^\ell := \begin{pmatrix} a_1^\ell \\ \vdots \\ a_N^\ell \\ a_{N+1}^\ell \end{pmatrix} \in \mathbb{R}^{N+1} \quad (40)$$

for $\ell = 1, \dots, L$, where $\bar{a}_{N+1}^\ell := x_N^{\ell-1}$ for $\ell = 2, \dots, L$ and $\bar{a}_{N+1}^1 := x_0$. Moreover, we introduce the following notations for the partial derivatives of the loss function

$$\Delta_p^{\text{out}} := \partial_p \mathcal{E}(a^{\text{out}}), \quad \text{for } p = 1, \dots, P, \quad (41)$$

$$\Delta_n^\ell := \partial_n \mathcal{E}(\bar{a}^\ell) = \partial_n \mathcal{E}(a^\ell), \quad \text{for } n = 1, \dots, N, \ell = 1, \dots, L, \quad (42)$$

$$\Delta_{N+1}^\ell := \partial_{N+1} \mathcal{E}(\bar{a}^\ell) = \partial_{N+1} \mathcal{E}(\bar{a}^\ell), \quad \text{for } \ell = 1, \dots, L. \quad (43)$$

The gradient of the loss function for the map representation (21)–(29) of the Fit-DNN with respect to the input, hidden, and output weights can be calculated using the following formulas:

- (i) We have $\Delta_p^{\text{out}} = \hat{y}_p - y_p$ if f^{out} is the softmax function and \mathcal{E} is the cross-entropy loss, or f^{out} is the identity function and \mathcal{E} is the mean-square loss.

(ii) The Δ -terms for the last hidden layer are

$$\Delta_{N+1}^L = \sum_{p=1}^P \Delta_p^{\text{out}} \sum_{j=1}^N e^{-\alpha\theta j} w_{pj}^{\text{out}}, \quad (44)$$

$$\Delta_n^L = \Phi f'(a_n^L) \sum_{p=1}^P \Delta_p^{\text{out}} \sum_{j=n}^N e^{-\alpha\theta(j-n)} w_{pj}^{\text{out}}, \quad \text{for } n = 1, \dots, N, \quad (45)$$

where $\Phi := \alpha^{-1}(1 - e^{-\alpha\theta})$.

(iii) The Δ -terms for the remaining hidden layers $\ell = L-1, \dots, 1$ are

$$\Delta_{N+1}^\ell = e^{-\alpha\theta N} \Delta_{N+1}^{\ell+1} + \sum_{i=1}^N \Delta_i^{\ell+1} \sum_{j=1}^N e^{-\alpha\theta j} w_{ij}^{\ell+1}, \quad (46)$$

$$\Delta_n^\ell = \Phi f'(a_n^\ell) \left[e^{-\alpha\theta(N-n)} \Delta_{N+1}^{\ell+1} + \sum_{i=1}^N \Delta_i^{\ell+1} \sum_{j=n}^N e^{-\alpha\theta(j-n)} w_{ij}^{\ell+1} \right], \quad (47)$$

for $n = 1, \dots, N$.

(iv) The partial derivatives of the loss function with respect to the output weights are

$$\frac{\partial \mathcal{E}}{\partial w_{pn}^{\text{out}}} = \Delta_p^{\text{out}} x_n^L, \quad \text{for } n = 1, \dots, N+1, \quad p = 1, \dots, P. \quad (48)$$

(v) The partial derivatives with respect to the hidden weights are

$$\frac{\partial \mathcal{E}}{\partial w_{nj}^\ell} = \Delta_n^\ell x_j^{\ell-1}, \quad \text{for } j = 1, \dots, N+1, \quad n = 1, \dots, N. \quad (49)$$

(vi) The partial derivatives in the input weights are

$$\frac{\partial \mathcal{E}}{\partial w_{nm}^{\text{in}}} = \Delta_n^1 g'(a_n^{\text{in}}) u_m, \quad \text{for } m = 1, \dots, M+1, \quad n = 1, \dots, N. \quad (50)$$

For a proof of statement (i) see e.g. [11]. The definition of Δ_p^{out} coincides with the definition of δ_p^{out} used for the formulation of the classical back-propagation algorithm.

In the following we give a technical proof of the statements (ii)-(viii).

(ii) The chain rule implies

$$\Delta_n^L = \partial_n \mathcal{E}(\bar{a}^L) = \sum_{p=1}^P \partial_p \mathcal{E}(a^{\text{out}}) \partial_n a_p^{\text{out}}(\bar{a}^L) = \sum_{p=1}^P \Delta_p^{\text{out}} \partial_n a_p^{\text{out}}(\bar{a}^L) \quad (51)$$

for $n = 1, \dots, N+1$. By Eq. (29) we have

$$a_p^{\text{out}} = \sum_{j=1}^{N+1} w_{pj}^{\text{out}} x_j^L, \quad (52)$$

where $x_{N+1}^L = 1$ is constant. The other node states x_n^L depend on the vector \bar{a}^L . Applying Eq. (23) and Eq. (24) iteratively and inserting $\bar{a}_{N+1}^L = x_N^{L-1}$ yields

$$x_j^L = e^{-\alpha\theta j} \bar{a}_{N+1}^L + \Phi \sum_{\nu=1}^j e^{-\alpha\theta(j-\nu)} f(\bar{a}_\nu^L). \quad (53)$$

Thus,

$$\partial_{N+1} a_p^{\text{out}}(\bar{a}^L) = \sum_{j=1}^N w_{pj}^{\text{out}} \partial_{N+1} x_j^L(\bar{a}^L) = \sum_{j=1}^N w_{pj}^{\text{out}} e^{-\alpha\theta j} \quad (54)$$

and for $n = 1, \dots, N$ we have

$$\partial_n a_p^{\text{out}}(\bar{a}^L) = \sum_{j=1}^N w_{pj}^{\text{out}} \partial_n x_j^L(\bar{a}^L) = \sum_{j=n}^N w_{pj}^{\text{out}} \Phi e^{-\alpha\theta(j-n)} f'(\bar{a}_n^L) \quad (55)$$

because

$$\partial_n x_j^L(\bar{a}^L) = \begin{cases} 0, & \text{if } j < n, \\ \Phi e^{-\alpha\theta(j-n)} f'(\bar{a}_n^L), & \text{if } j \geq n. \end{cases} \quad (56)$$

Inserting Eq. (54) into Eq. (51) yields Eq. (44) and inserting Eq. (55) into Eq. (51) yields Eq. (45).

(iii) The chain rule implies

$$\begin{aligned}
\Delta_n^\ell &= \partial_n \mathcal{E}(\bar{a}^\ell) \\
&= \partial_{N+1} \mathcal{E}(\bar{a}^{\ell+1}) \partial_n \bar{a}_{N+1}^{\ell+1}(\bar{a}^\ell) + \sum_{i=1}^N \partial_i \mathcal{E}(\bar{a}^{\ell+1}) \partial_n \bar{a}_i^{\ell+1}(\bar{a}^\ell) \\
&= \Delta_{N+1}^{\ell+1} \partial_n \bar{a}_{N+1}^{\ell+1}(\bar{a}^\ell) + \sum_{i=1}^N \Delta_i^{\ell+1} \partial_n \bar{a}_i^{\ell+1}(\bar{a}^\ell)
\end{aligned} \tag{57}$$

for $n = 1, \dots, N+1$. From Eq. (23) and Eq. (24) follows

$$\bar{a}_{N+1}^{\ell+1} = x_N^\ell = e^{-\alpha\theta N} \bar{a}_{N+1}^\ell + \Phi \sum_{\nu=1}^N e^{-\alpha\theta(N-\nu)} f(\bar{a}_\nu^\ell) \tag{58}$$

and hence

$$\partial_{N+1} \bar{a}_{N+1}^{\ell+1}(\bar{a}^\ell) = e^{-\alpha\theta N} \tag{59}$$

and

$$\partial_n \bar{a}_{N+1}^{\ell+1}(\bar{a}^\ell) = \Phi e^{-\alpha\theta(N-n)} f'(\bar{a}_n^\ell), \tag{60}$$

for $n = 1, \dots, N$. Furthermore, for $i = 1, \dots, N$, Eq. (28) implies

$$\bar{a}_i^{\ell+1} = \sum_{j=1}^{N+1} w_{ij}^{\ell+1} x_j^\ell, \tag{61}$$

where $x_{N+1}^\ell = 1$ is constant and applying Eq. (21)–(24) iteratively yields

$$x_j^\ell = e^{-\alpha\theta j} \bar{a}_{N+1}^\ell + \Phi \sum_{\nu=1}^j e^{-\alpha\theta(j-\nu)} f(\bar{a}_\nu^\ell). \tag{62}$$

This implies

$$\partial_{N+1} \bar{a}_i^{\ell+1}(\bar{a}^\ell) = \sum_{j=1}^N w_{ij}^{\ell+1} \partial_{N+1} x_j^\ell(\bar{a}^\ell) = \sum_{j=1}^N w_{ij}^{\ell+1} e^{-\alpha\theta j} \tag{63}$$

and

$$\partial_n \bar{a}_i^{\ell+1}(\bar{a}^\ell) = \sum_{j=1}^N w_{ij}^{\ell+1} \partial_n x_j^\ell(\bar{a}^\ell) = \sum_{j=n}^N w_{ij}^{\ell+1} \Phi e^{-\alpha\theta(j-n)} f'(\bar{a}_n^\ell) \tag{64}$$

for $n = 1, \dots, N$, because

$$\partial_n x_j^\ell(\bar{a}^\ell) = \begin{cases} 0, & \text{if } j < n, \\ \Phi e^{-\alpha\theta(j-n)} f'(\bar{a}_n^\ell), & \text{if } j \geq n. \end{cases} \tag{65}$$

Inserting (59) and (63) into (57) yields (46). Inserting (60) and (64) into (57) yields (47).

(iv)-(vi) These statements follow immediately from the chain rule:

For the partial derivatives of with respect to the output weights, we obtain

$$\frac{\partial \mathcal{E}}{\partial w_{pn}^{\text{out}}} = \partial_p \mathcal{E}(a^{\text{out}}) \frac{\partial a_p^{\text{out}}}{\partial w_{pn}^{\text{out}}} = \Delta_p^{\text{out}} x_n^L, \tag{66}$$

for $n = 1, \dots, N+1$, $p = 1, \dots, P$.

For the partial derivatives with respect to the hidden weights, it holds

$$\frac{\partial \mathcal{E}}{\partial w_{nj}^\ell} = \partial_n \mathcal{E}(a^\ell) \frac{\partial a_n^\ell}{\partial w_{nj}^\ell} = \Delta_n^\ell x_j^{\ell-1}, \tag{67}$$

for $j = 1, \dots, N+1$, $n = 1, \dots, N$.

For the partial derivatives with respect to the input weights, the chain rule implies

$$\frac{\partial \mathcal{E}}{\partial w_{nm}^{\text{in}}} = \partial_n \mathcal{E}(a^1) \frac{\partial a_n^1}{\partial w_{nm}^{\text{in}}} = \Delta_n^1 g'(a_n^{\text{in}}) \frac{\partial a_n^{\text{in}}}{\partial w_{nm}^{\text{in}}} = \Delta_n^1 g'(a_n^{\text{in}}) u_m, \tag{68}$$

for $m = 1, \dots, M+1$, $n = 1, \dots, N$.

The formulas for Δ_n^ℓ , Eq. (46) and (47), contain weighted sums over the hidden weights. These sums can be substituted as follows:

$$\sum_{j=1}^N e^{-\alpha\theta j} w_{ij}^{\ell+1} = \sum_{\substack{d=1 \\ 1 \leq i-n'_d \leq N}}^D e^{-\alpha\theta(i-n'_d)} v_{d,i}^{\ell+1} \tag{69}$$

and similarly

$$\sum_{j=n}^N e^{-\alpha\theta(j-n)} w_{ij}^{\ell+1} = \sum_{\substack{d=1 \\ n \leq i-n'_d \leq N}}^D e^{-\alpha\theta(i-n'_d-n)} v_{d,i}^{\ell+1}. \quad (70)$$

The equations (69) and (70) follow from the definition of the hidden weight matrices, Eq. (20), which yields

$$w_{i,i-n'_d}^{\ell} = v_{d,i}^{\ell} = \mathcal{M}_d^{\ell}(i\theta) \quad (71)$$

and $w_{ij}^{\ell} = 0$ for all $j \notin \{i - n'_d \mid d = 1, \dots, D\} \cup \{N + 1\}$. Replacing the sums over the index j by sums over the index d reduces the computational costs of the formulas significantly.

4 Time signals of the Fit-DNN

Figure 8 illustrates how the Fit-DNN processes information by showing its time signals. Panel (a) illustrates the processing of an input image, in this case an image of the handwritten number 4, to obtain the data signal $J(t)$, which is a step function with step size θ . First, the extended input vector u is multiplied by the trained input matrix W^{in} . Then an input preprocessing function g is applied element-wise to the entries of the obtained vector. The resulting values are the step heights of the data signal $J(t)$.

Panel (b) shows the internal processes in the hidden layers. From top to bottom we plot:

- the state of the system $x(t)$,
- the signal $a(t)$,
- the signal $a(t)$ decomposed into the positive and the negative parts of its components (i.e. the data signal, the modulated feedback signals, and the bias signal) indicated by their corresponding color,
- the data signal $J(t)$,
- the delayed feedback signals $x(t - \tau_d)$ (grey),
- the trained modulation functions $M_d(t)$ (colored),
- and the bias $b(t)$.

The signal $a(t)$ for the first hidden layer, $0 \leq t \leq T$, coincides with the data signal $J(t)$. For the remaining hidden layers, the signal $a(t)$ is a sum of the modulated feedback signals and the bias.

Panel (c) illustrates the output layer. The vector x_L , containing the values of $x(t)$ sampled at $t = (L-1)T + \theta, \dots, (L-1)T + N\theta$, is multiplied by the trained output matrix W^{out} to obtain the output activation vector. Then the softmax function is applied to obtain the output vector y^{out} . In this case, the Fit-DNN correctly identifies the input image as the number 4.

The training process, which lead to the trained system depicted in Fig. 8, is shown in a video, which is attached as additional Supplementary Information.

References

- [1] Krizhevsky, A. Learning multiple layers of features from tiny images. *University of Toronto* (2012).
- [2] Netzer, Y. *et al.* Reading digits in natural images with unsupervised feature learning. *NIPS* (2011).
- [3] Lecun, Y., Bottou, L., Bengio, Y. & Haffner, P. Gradient-based learning applied to document recognition. *Proceedings of the IEEE* **86**, 2278–2324 (1998).
- [4] Xiao, H., Rasul, K. & Vollgraf, R. Fashion-mnist: a novel image dataset for benchmarking machine learning algorithms. Preprint at <https://arxiv.org/abs/1708.07747> (2017).
- [5] Hale, J. K. & Lunel, S. M. V. *Introduction to Functional Differential Equations* (Springer, New York, 1993).
- [6] Diekmann, O., Verduyn Lunel, S. M., van Gils, S. A. & Walther, H.-O. *Delay Equations* (Springer, New York, 1995).
- [7] Wu, J. *Introduction to Neural Dynamics and Signal Transmission Delay* (Walter de Gruyter, Berlin, Boston, 2001).
- [8] Erneux, T., Javaloyes, J., Wolfrum, M. & Yanchuk, S. Introduction to Focus Issue: Time-delay dynamics. *Chaos: An Interdisciplinary Journal of Nonlinear Science* **27**, 114201 (2017).
- [9] Hart, J. D., Schmadel, D. C., Murphy, T. E. & Roy, R. Experiments with arbitrary networks in time-multiplexed delay systems. *Chaos: An Interdisciplinary Journal of Nonlinear Science* **27**, 121103 (2017).
- [10] Hart, J. D., Larger, L., Murphy, T. E. & Roy, R. Delayed dynamical systems: networks, chimeras and reservoir computing. *Philosophical Transactions of the Royal Society A: Mathematical, Physical and Engineering Sciences* **377**, 20180123 (2019).
- [11] Bishop, C. M. *Pattern Recognition and Machine Learning* (Springer, New York, 2006).

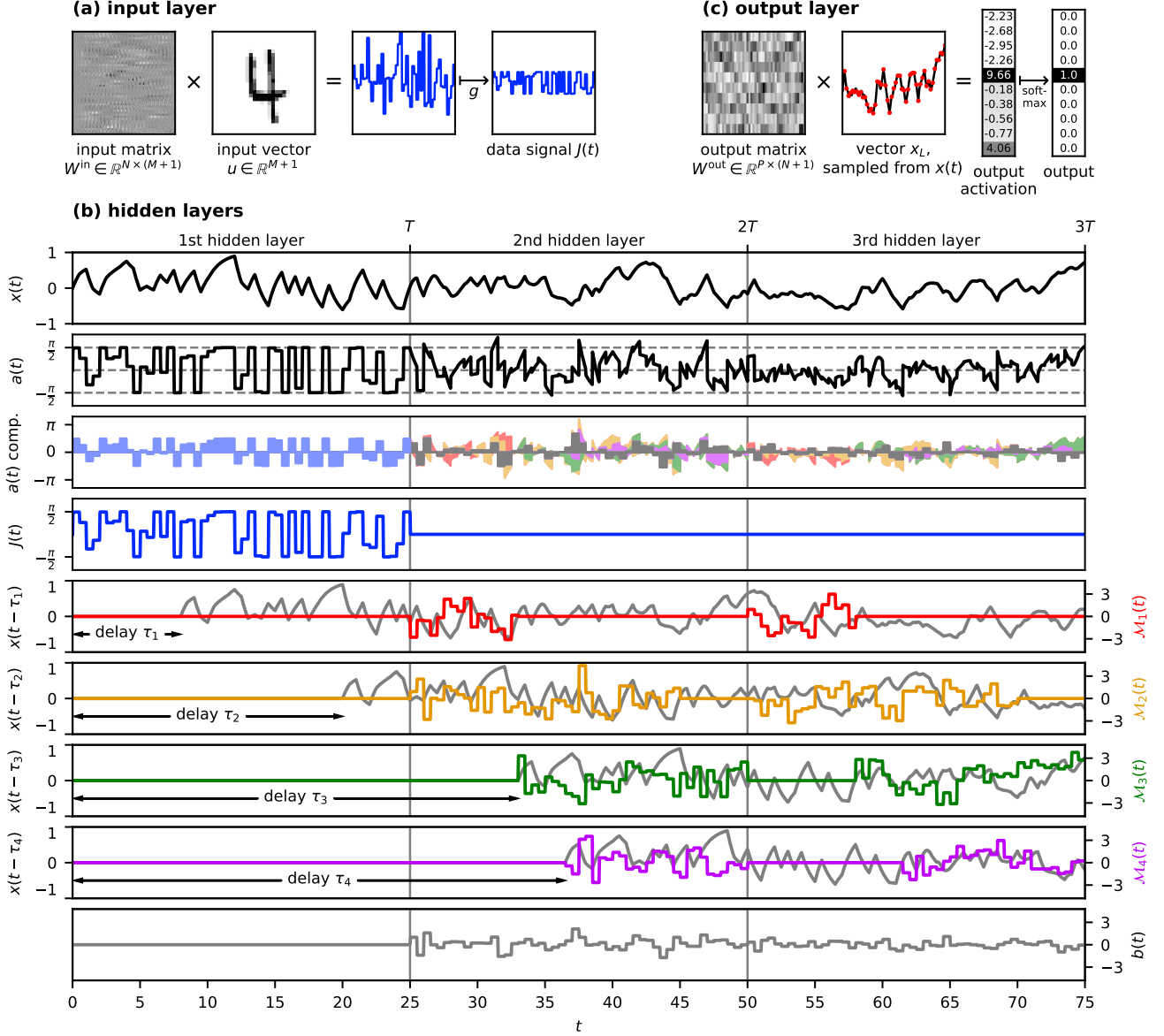


Figure 8: Time signals of the Fit-DNN after training. Panel (a) illustrates the processing of an input image to obtain the data signal $J(t)$. Panel (b) shows the internal processes of the hidden layers: the state variable of the system $x(t)$, and the signal $a(t)$, which consists of the data signal $J(t)$, the delayed feedback signals $x(t - \tau_d)$ multiplied by the modulation functions $M_d(t)$, and the bias signal $b(t)$. Panel (c) illustrates the output layer.